

# Accurate lubrication corrections for spherical and non-spherical particles in discretized fluid simulations

F. Janoschek,<sup>1,\*</sup> J. Harting,<sup>1,2,†</sup> and F. Toschi<sup>1,3,‡</sup>

<sup>1</sup>*Department of Applied Physics, Eindhoven University of Technology,  
P. O. Box 513, 5600 MB Eindhoven, The Netherlands*

<sup>2</sup>*Institute for Computational Physics, University of Stuttgart, Allmandring 3, 70569 Stuttgart, Germany*

<sup>3</sup>*CNR-IAC, Via dei Taurini 19, 00185 Rome, Italy*

(Dated: August 30, 2013)

Discretized fluid solvers coupled to a Newtonian dynamics method are a popular tool to study suspension flow. As any simulation technique with finite resolution, the lattice Boltzmann method, when coupled to discrete particles using the momentum exchange method, resolves the diverging lubrication interactions between surfaces near contact only insufficiently. For spheres, it is common practice to account for surface-normal lubrication forces by means of an explicit correction term. A method that additionally covers all further singular interactions for spheres is present in the literature as well as a link-based approach that allows for more general shapes but does not capture non-normal interactions correctly. In this paper, lattice-independent lubrication corrections for aspherical particles are outlined, taking into account all leading divergent interaction terms. An efficient implementation for arbitrary spheroids is presented and compared to purely normal and link-based models. Good consistency with Stokesian dynamics simulations of spheres is found. The non-normal interactions affect the viscosity of suspensions of spheres at volume fractions  $\Phi \geq 0.3$  but already at  $\Phi \geq 0.2$  for spheroids. Regarding shear-induced diffusion of spheres, a distinct effect is found at  $0.1 \leq \Phi \leq 0.5$  and even increasing the resolution of the radius to 8 lattice units is no substitute for an accurate modeling of non-normal interactions.

PACS numbers: 47.11.-j, 47.57.E-, 47.15.-x, 47.11.Qr

## I. INTRODUCTION

The dynamics of particles suspended in a fluid plays an important role for a large set of problems ranging from sedimentation and fluidization processes in industrial-scale chemical reactors to capillary blood flow in human microcirculation. Especially the shear-induced mass transport in suspensions of non-spherical particles, such as blood cells, has grown to a very active field of research recently [1–6]. All these examples have in common that the gap between the surfaces of either two particles or between one particle and the geometry confining the flow frequently becomes small as compared to the particle size. The consequence are hydrodynamic short-range interactions mediated by the interstitial fluid that increase in strength as the distance of the surfaces decreases and that can play an important role in suspension rheology [7] but also in the dynamics of the suspended particles themselves [8]. The smallness of the gap between the surfaces allows for the assumption of Stokes flow. Thus, the forces and torques on the surfaces appear as linear functions of their translation and rotation velocities which is most conveniently formulated in terms of a resistance matrix. Furthermore, the smallness of the gap allows a lubrication-theoretical treatment of the interactions. While the lubrication limit is treated already by

Goldman *et al.* [9] in the case of a sphere next to a plane wall, the work by Cox [10] is the first to consider arbitrary yet smooth and convex surfaces. Approximating the surfaces at their points of closest approach as polynomials of second order, Cox [10] studies the divergence behavior of the resistance matrix for vanishing gap widths  $h$  and presents explicit expressions for the leading-order terms of most of the matrix elements. It is found that while the surface-normal force induced by a relative translation of the surfaces along the same direction diverges as  $h^{-1}$ , all other interactions show a weaker divergence proportional to  $\ln h$  or even remain finite. Claeys and Brady [11] complete the study by Cox [10], taking into account the third- and fourth-order expansion coefficients of the local surface geometry which are required to compute all diverging terms for all matrix elements. The results are employed later for the Stokesian dynamics simulation of suspensions of prolate spheroids by the same authors [12]. A computationally more efficient model for oblate spheroids that neglects long-range hydrodynamic interactions and for the computation of lubrication interactions locally approximates the interacting surfaces as spheres is proposed by Bertevras *et al.* [13].

Stokesian dynamics simulations are restricted to the creeping flow regime. To model suspension flow at finite Reynolds numbers, the lattice Boltzmann (LB) method [14], especially when used in connection with the momentum exchange method originating from Ladd [15, 16], has emerged as an increasingly popular technique during the last two decades that further allows for a comparably easy parallel implementation and for complex

---

\* f.j@noschek.de

† j.harting@tue.nl

‡ f.toschi@tue.nl

boundary conditions [17, 18]. Since the method describes the fluid only at discrete nodes of a lattice with finite spatial resolution it cannot account for lubrication interactions at arbitrarily small particle separations directly. Already resolving them at separations of  $\sim 10\%$  of the particle radius would require lattice resolutions that are finer and computationally more expensive than the ones necessary to obtain accurate drag coefficients and particle interactions at larger separations [16, 17, 19, 20]. Similar problems arise also in other simulation methods with finite resolution, such as finite element methods [21], stochastic rotation dynamics [22], or dissipative particle dynamics [23]. In the case of spherical particles it is common practice to address these issues by correcting the LB method for particles near contact with the asymptotic expressions known from lubrication theory. While many implementations correct only for normal lubrication forces resulting from a central approach of the spheres [24–26], Nguyen and Ladd [27] account for the leading divergence terms of the weaker non-normal interactions as well. To the best of the authors’ knowledge, a comparably accurate method for aspherical particles does not exist up to now. In fact, present applications of the LB and momentum exchange method to suspensions of aspherical particles often do not account for lubrication interactions explicitly [28], ignore the torque resulting from asymmetric encounters [29], or defer the description of short-range interactions to an empirical model [30]. On the other hand, Ding and Aidun [31] introduce a method for lubrication correction that is based on the interconnecting lattice links between particles near contact and thus is directly applicable to aspherical particles. The method is employed later in simulations of deformable particles [32]. More recently, however, drawbacks of the link-based approach are stated to be the demand for a relatively large minimum lattice resolution [18] and the misestimation of non-normal lubrication interactions [33].

It therefore appears that the present literature shows some uncertainty regarding the degree of accuracy actually required from lubrication corrections in LB simulations as well as regarding how to implement a sufficiently accurate lubrication model for aspherical particles. The goal of this work is to mitigate these uncertainties. In section II below the LB method and the momentum exchange method are briefly introduced, followed by an outline of contact-based lubrication corrections for spheres and of a link-based lubrication model. In section III the implementation of accurate lubrication corrections for aspherical particles following the analytical work by Cox [10] and by Claeys and Brady [11] is demonstrated for the case of spheroids. Section IV compares the different lubrication models with respect to the accuracy of two-particle interactions and with respect to the shear-induced diffusion and the viscosity of a suspension as examples for one observable that examines the dynamics of single particles and one averaged observable, all with the focus on the effect of non-normal lubrication corrections. Conclusions are drawn in section V. The appendix

provides a compilation of the diverging terms in the resistance matrix that are given already by Cox [10] and the remaining leading terms first computed by Claeys and Brady [11].

## II. LATTICE BOLTZMANN METHOD FOR SUSPENSIONS OF SOLID PARTICLES

Historically, the LB method originates from lattice gas cellular automata. A comprehensive introduction is available in the book by Succi [14]. Time  $t$  is discretized in steps  $\delta t = 1$ , space in positions  $\mathbf{x}$  on a regular lattice defined by a finite set of  $q$  discrete velocity vectors  $\mathbf{c}_r$  with  $r = 1, \dots, q$ . Fluid particles at position  $\mathbf{x}$  and time  $t$  traveling along  $\mathbf{c}_r$  are represented by the discretized single-particle distribution function  $n_r(\mathbf{x}, t)$ . The algorithm to propagate  $n_r(\mathbf{x}, t)$  in time prescribes the repeated consecutive execution of the advection step

$$n_r(\mathbf{x} + \mathbf{c}_r, t + \delta t) = n_r^*(\mathbf{x}, t) \quad (1)$$

and the collision step

$$n_r^*(\mathbf{x}, t) = n_r(\mathbf{x}, t) - \Omega, \quad (2)$$

the latter producing the post-collision distribution  $n_r^*(\mathbf{x}, t)$ . Eq. 2 and Eq. 1 together form the LB equation. For the sake of simplicity, the Bhatnagar-Gross-Krook collision term

$$\Omega = \frac{n_r(\mathbf{x}, t) - n_r^{\text{eq}}(\rho(\mathbf{x}, t), \mathbf{u}(\mathbf{x}, t))}{\tau} \quad (3)$$

with a single-relaxation time  $\tau$  is employed. It relies on a second-order expansion of the Maxwell-Boltzmann equilibrium distribution

$$n_r^{\text{eq}}(\rho, \mathbf{u}) = \rho \alpha_{c_r} \left[ 1 + \frac{\mathbf{c}_r \mathbf{u}}{c_s^2} + \frac{(\mathbf{c}_r \mathbf{u})^2}{2c_s^4} - \frac{\mathbf{u}^2}{2c_s^2} \right] \quad (4)$$

with a speed of sound  $c_s$ . The local density

$$\rho(\mathbf{x}, t) = \sum_r n_r(\mathbf{x}, t) \quad (5)$$

and velocity

$$\mathbf{u}(\mathbf{x}, t) = \frac{\sum_r n_r(\mathbf{x}, t) \mathbf{c}_r}{\rho(\mathbf{x}, t)} \quad (6)$$

are calculated as moments of the fluid distribution. In the following, the three-dimensional D3Q19 lattice [34] is applied for which  $q = 19$  and the lattice weights

$$\alpha_{c_r} = \begin{cases} 1/3 & \text{for } c_r = 0 \\ 1/18 & \text{for } c_r = 1 \\ 1/36 & \text{for } c_r = \sqrt{2} \end{cases}. \quad (7)$$

In a Chapman-Enskog expansion it can be shown that  $\mathbf{u}(\mathbf{x}, t)$  as obtained from the method follows the incompressible Navier-Stokes equations with a kinematic viscosity  $\nu = (\tau - \frac{1}{2}) c_s^2$  in the limit of small Mach numbers  $\text{Ma} = u/c_s$  with  $c_s = 1/\sqrt{3}$  [34].

In the momentum exchange method [17], particle volumes of in principle arbitrary shape are discretized on the lattice as outlined in Fig. 1(a) and coupled to the fluid via the links crossing the resulting particle-fluid interface. While the original work [15, 16] treats particles as fluid-filled shells, the inner fluid is removed in later implementations [27, 35] including the one described here. A no-slip boundary moving with velocity  $\mathbf{v}_b$  is established by a mid-link bounce-back rule

$$n_r(\mathbf{x} + \mathbf{c}_r, t + \delta t) = n_{\bar{r}}^*(\mathbf{x} + \mathbf{c}_r, t) + C \quad (8)$$

with a first-order velocity correction [15]

$$C = \frac{2\alpha_{c_r}}{c_s^2} \rho(\mathbf{x} + \mathbf{c}_r, t) \mathbf{c}_r \mathbf{v}_b \quad (9)$$

that replaces Eq. 1 where required to prevent advection out of a particle site  $\mathbf{x}$ . The index  $\bar{r}$  is defined by  $\mathbf{c}_{\bar{r}} \equiv -\mathbf{c}_r$ . Eq. 8 with Eq. 9 is easily shown to be consistent with Eq. 4. The reduction of fluid momentum by each bounce-back process

$$d\mathbf{p} = (2n_{\bar{r}} + C) \mathbf{c}_{\bar{r}}, \quad (10)$$

is transferred to the respective particle. According to the choice of unit time steps it is equal to the resulting force. Eq. 10 can be seen as a discretized traction vector and is therefore used to compute the hydrodynamic force and torque on the particle. When, due to particle motion, new fluid sites are covered, the fluid at those sites is deleted. When a site formerly occupied by a particle is freed, new fluid is created according to Eq. 4 with an average fluid density  $\rho$  and  $\mathbf{u}$  estimated according to the rigid-body motion of the particle. Momentum conservation is ensured instantaneously by an appropriate force on the particle. The data published by Ladd [16] for an input radius  $R = 4.5$  defining the discretization on the lattice suggests that the effective hydrodynamic radius  $R^*$  defined via the drag coefficient deviates least from  $R$  for a relaxation time somewhat below  $\tau = 1$ . In the following,  $\tau = 1$  is chosen and no effort is made to recalibrate particle radii using  $R^*$ . For spherical particles both the relative deviations of the translational drag coefficient from the expected value and its fluctuations due to the aforementioned discretization changes are found to be below 10% already at a resolution of the sphere radius of only  $R = 2.5$  lattice sites [16, 36].

Problems arise when particle surfaces approach closely. The short-range interactions are truthfully described down to a gap width of only about 1 lattice spacing [16]. At shorter distances, the expected divergence is not reproduced, instead the friction coefficients stay approximately constant to the value achieved at a distance of 1 [16]. The observation can be understood as depicted in Fig. 1(a): a gap width between both surfaces of about 1 lattice spacing is the distance below which direct links between both particles emerge. Further approach does not lead to changes in the fluid site configuration in the gap which could cause an increase in the interaction forces.

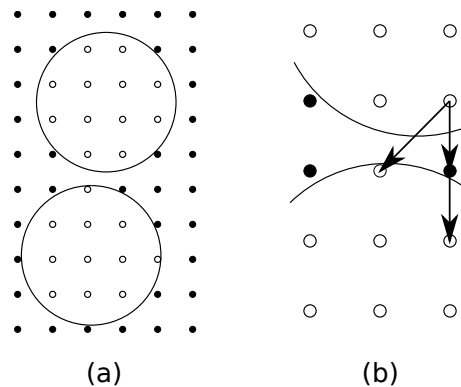


FIG. 1. (a) The discretized representation on the lattice leads to unresolved short-range hydrodynamic interactions between particles near contact. In the link-wise approach by Ding and Aidun [31], correction forces are computed for single links and for pairs of identical links connecting the particles as visualized in (b). For clarity, not all interconnecting links are drawn.

Ladd addresses the issue later [17, 24] by employing the dominating divergence term  $\sim h^{-1}$  of the normal force induced by the central approach of two spheres at a gap distance  $h = r_{ij} - 2R$  as a correction

$$\mathbf{f}_{ij} = -\mathbf{f}_{ji} = -\frac{3\pi\mu R^2}{2} \hat{\mathbf{r}}_{ij} \hat{\mathbf{r}}_{ij} \cdot (\mathbf{v}_i - \mathbf{v}_j) \left[ \frac{1}{h} - \frac{1}{\Delta_c} \right] \quad (11)$$

to the hydrodynamic force on sphere  $i$  due to another sphere  $j$  for which  $h < \Delta_c$ . The center displacement is  $\mathbf{r}_{ij} = \mathbf{r}_i - \mathbf{r}_j$ , the related unit vector  $\hat{\mathbf{r}}_{ij} = \mathbf{r}_{ij}/r_{ij}$ ,  $\mathbf{v}_i$  and  $\mathbf{v}_j$  denote the particles' translational velocities, and  $\mu = \rho\nu$  refers to the dynamic viscosity of the suspending medium. As a cut-off parameter,  $\Delta_c$  represents the separation below which the LB method alone does not sufficiently cover hydrodynamic interactions anymore.  $\Delta_c$  is a function of  $\tau$  [27]. For  $\tau = 1$ , a value  $\Delta_c = 2/3$  is suggested [17, 27]. Corrections equivalent to Eq. 11 for spheres of possibly differing radii are introduced also for the forces and torques resulting from rotation and non-normal translation by Nguyen and Ladd [27]. These, however, diverge only as  $\ln h$  and require separate cut-off parameters [27].

An implicit integration scheme for the particle trajectories is one way to maintain numerical stability in the presence of clusters of particles with strong lubrication interactions [17, 27]. In the implementation employed here, the time step for the particle update is decoupled from the LB time step instead which allows its reduction, to typically 1/10: while the forces due to the momentum exchanged with the LB fluid via Eq. 10 remain constant over one LB step, the particle positions and velocities are updated in accordance with the strongly varying explicit lubrication forces at a finer temporal resolution.

Ding and Aidun [31] propose an alternative method for lubrication corrections that is based on the interconnecting lattice links between particles and therefore does

not require analytical knowledge of the particles' asymptotic resistance functions [18]. In this method, a partial lubrication force

$$\mathbf{d}\mathbf{f}_{ij} = -\mathbf{d}\mathbf{f}_{ji} = -\frac{3\bar{q}\mu}{2c_r^2\lambda^*}\hat{\mathbf{c}}_r\hat{\mathbf{c}}_r\cdot(\mathbf{v}_{b_i}-\mathbf{v}_{b_j})\left[\frac{1}{h^{*2}}-\frac{1}{c_r^2}\right] \quad (12)$$

with  $\hat{\mathbf{c}}_r = \mathbf{c}_r/c_r$  is applied locally to particle  $i$  for all links  $\mathbf{c}_r$  that end on a site belonging to  $i$  and stem from either a site of particle  $j$  or a fluid site at the center of two links  $2\mathbf{c}_r$  originating from  $j$ . Both possibilities are outlined in Fig. 1(b). The gap distance  $h^*$  is the distance between the intersections of both theoretical particle surfaces with the lattice link or the pair of links and therefore is typically larger than the actual minimum gap. The correction is applied only where  $h^* < c_r$ . The velocities  $\mathbf{v}_{b_i}$  and  $\mathbf{v}_{b_j}$  at the intersection points are computed from the particles' rigid body motion. Different from Eq. 11, the model can produce non-central forces depending on the link direction  $\mathbf{c}_r$ . The curvature  $\lambda^*$  is obtained as the mean of both surfaces and  $\bar{q} = 0.6$  is an empiric weighting factor [31]. Despite its generality, the model is applied and validated initially only in the case of normal approach of spheres and cylinders towards each other and towards a flat wall [31]. For centrally approaching spheres, analytical consistency with the known asymptotic behavior is demonstrated [31].

Eq. 12 is applied to deformable particles later [32] but Clausen [33] notes an erroneous divergence of tangential interactions as  $h^{-1}$  which he fixes, along with further modifications, by the introduction of an average normal direction  $\mathbf{n}_{\text{avg}}$  of the surfaces. Both the difference of the boundary velocities and the link-wise gap are projected along  $\mathbf{n}_{\text{avg}}$  and the resulting force is applied in the same direction. Thereby, however, locally tangential lubrication corrections are removed. Moreover, the discretization of lubrication interactions onto interconnecting lattice links that appear and vanish as particles move is found to cause instabilities [33] that apparently prevent usage of the link-wise model in at least some of the subsequent work [2].

### III. CONTACT-BASED LUBRICATION CORRECTIONS FOR SPHEROIDS

Though many of the following ideas could be applied to particles of other convex shapes as well, spheroids with half axes  $R_{\parallel}$  and  $R_{\perp}$  parallel and perpendicular to their axis of rotational symmetry will be treated here. A convenient parametrization of the surface is

$$\tilde{\mathbf{y}}(p, q) = \begin{pmatrix} R_{\perp} \cos p \cos q \\ R_{\perp} \cos p \sin q \\ R_{\parallel} \sin p \end{pmatrix}, \quad (13)$$

where the tilde indicates a representation in the body-fixed reference frame where the origin is at the center of the particle and the  $\tilde{y}_3$ -direction oriented along its axis of

rotational symmetry. For symmetry reasons, the directions of principal curvature are the tangential directions

$$\tilde{\mathbf{s}}_1(p, q) = \partial_p \tilde{\mathbf{y}}(p, q) \quad \text{and} \quad \tilde{\mathbf{s}}_2(p, q) = \partial_q \tilde{\mathbf{y}}(p, q). \quad (14)$$

The respective radii of curvature

$$S_1(p) = \frac{s_1(p)^3}{R_{\parallel}R_{\perp}} \quad \text{and} \quad S_2(p) = \frac{R_{\perp}s_1(p)}{R_{\parallel}}, \quad (15)$$

with

$$s_1(p) = |\tilde{\mathbf{s}}_1(p)| = \sqrt{R_{\perp}^2 \sin^2 p + R_{\parallel}^2 \cos^2 p} \quad (16)$$

can be obtained from a second-order expansion of Eq. 13.

#### A. Minimum gap between two spheroids

The strong dependence of lubrication interactions on the minimum separation between two particles  $i$  and  $j$  requires precise knowledge of the magnitude and direction of the minimum gap vector  $\mathbf{h}$ . For two spheres with radii  $R_i$  and  $R_j$ , the result trivially is  $\mathbf{h} = -(r_{ij} - R_i - R_j)\hat{\mathbf{r}}_{ij}$ , where the minus sign ensures a direction away from particle  $i$ . Already for spheroids the problem in general is considerably more intricate. One solution is to follow the iterative procedure presented by Lin and Han [37] for the distance between two ellipsoids. As illustrated in Fig. 2, the method involves the re-positioning of tangent spheres along the inner surface of each ellipsoid to minimize the distance of the sphere centers and thus the gap between the ellipsoids. A sufficient requirement for convergence of the method is that each sphere is completely contained in the respective ellipsoid [37]. This is achieved easily if the radius is chosen as the minimum radius of curvature

$$\bar{S} = \begin{cases} R_{\parallel}^2/R_{\perp} & \text{for } R_{\parallel} < R_{\perp} \\ R & \text{for } R_{\parallel} = R_{\perp} = R \\ R_{\perp}^2/R_{\parallel} & \text{for } R_{\parallel} > R_{\perp} \end{cases}. \quad (17)$$

Initially, the spheres are placed tangent in the intersection points of the spheroid surfaces with the line connecting the spheroid centers. In the iteration, the tangent points  $\mathbf{y}_i$  and  $\mathbf{y}_j$  are repeatedly updated to become the intersections of the spheroid surfaces with the line connecting the current centers  $\mathbf{z}_i$  and  $\mathbf{z}_j$  of the spheres. The iteration stops once the angles  $\theta_i$  and  $\theta_j$  between the outward pointing surface unit normals  $\hat{\mathbf{n}}_i$  in  $\mathbf{y}_i$  and  $\hat{\mathbf{n}}_j$  in  $\mathbf{y}_j$  and the vector  $\mathbf{z}_{ij} = \mathbf{z}_i - \mathbf{z}_j$  between the sphere centers approximate zero. The converged surface positions of minimum distance are referred to as  $\mathbf{y}_i^*$  and  $\mathbf{y}_j^*$  in the following. Practically, the convergence criterion is implemented as the requirement that both

$$\cos \theta_i = -\hat{\mathbf{n}}_i \cdot \hat{\mathbf{z}}_{ij} > 1 - \epsilon, \quad (18)$$

with  $\hat{\mathbf{z}}_{ij} = \mathbf{z}_{ij}/z_{ij}$  and Eq. 18 with indices  $i$  and  $j$  swapped hold. Due to the small magnitude of  $\partial \cos \theta_i / \partial \theta_i$

near  $\theta_i = 0$ , a rather low value of  $\epsilon = 10^{-6}$  is chosen to ensure accuracy. The resulting gap vector is  $\mathbf{h} = -(z_{ij} - 2\bar{S})\hat{\mathbf{z}}_{ij}$ .

For overlapping particles, Lin and Han [37] effectively state that  $h = 0$  and abstain from a further treatment. When implemented accordingly, their method as described above is, however, stable also for configurations where particles overlap to an amount small as compared to their radii of curvature. Then,  $\mathbf{h}$  still points from the bulk of particle  $i$  to  $j$  but the scalar gap  $z_{ij} - 2\bar{S}$  is negative. This is an important feature that could be used to model elastic contact forces but also to enhance the stability of dense simulations of infinitely stiff particles with a finite time step where minimal amounts of overlap are surely undesired but sometimes inevitable.

Eq. 17 ensures that the tangent spheres assumed in the algorithm lie within the respective spheroids which is noted to be sufficient for convergence but not necessarily optimal with respect to the number of iterations required [37]. In many cases typical for the spheroids simulated here, convergence can indeed be speeded up dramatically by adjusting  $\bar{S}$  for each surface to the smaller of the two local principal radii of curvature in Eq. 15. Thus, a two-fold strategy is being followed: first, up to  $N_1$  iterations with  $\bar{S} = \min\{S_1(p), S_2(p)\}$  are performed. Since due to the potentially enlarged  $\bar{S}$  and the allowance for overlap a meaningful result is not guaranteed, two consistency checks are performed whenever Eq. 18 indicates convergence: it is required that  $\hat{\mathbf{n}}_j \cdot \mathbf{r}_{ij} > 0$  and  $\hat{\mathbf{n}}_i \cdot \mathbf{r}_{ij} < 0$  so the outward-directed surface normals point towards the center of the other particle. In case of overlap,  $\mathbf{y}_i^*$  has to be contained within particle  $j$  and vice versa. If at least one of the conditions fails or convergence is not achieved yet, the algorithm restarts with the more conservative  $\bar{S}$  from Eq. 17 for a maximum of  $N_2$  iterations. Here,  $N_1 = 10$  and  $N_2 = 1000$  is chosen as a set of values that for particles with aspect ratio  $\Lambda = R_{\parallel}/R_{\perp} = 1/3$  results in an average total number of iterations per gap computation of almost 40. This is a reduction of about 30% as compared to only one iteration with fixed radii defined by Eq. 17. So far, no configuration without significant overlap is known where the combined procedure with these parameters fails to converge.

With a cut-off gap such as  $\Delta_c$  in Eq. 11, it is necessary to determine  $\mathbf{h}$  once during every (particle-)time step for every pair of particles with a minimum separation that is potentially smaller than  $\Delta_c$ . All pairs with a center distance  $r_{ij} > 2 \max\{R_{\parallel}, R_{\perp}\} + \Delta_c$  can clearly be excluded. A computation is unnecessary also if  $r_{ij} > \max\{R_{\parallel}, R_{\perp}\} + \Delta_c \equiv R_c$  but at the same time particle  $i$  has no intersection with a plane normal to  $\mathbf{r}_{ij}$  in a distance of  $R_c$  away from  $\mathbf{r}_j$  in the direction of  $i$  or vice versa. This can be tested in a comparably inexpensive way and avoids unneeded computations of  $\mathbf{h}$ , especially in the case of highly aspherical particles. A further very effective approach for optimization consists in starting the iteration to obtain  $\mathbf{h}$  not from the particle centers as explained above but using the converged tangent po-

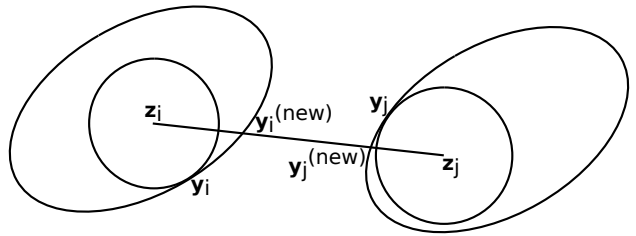


FIG. 2. Two-dimensional outline of the iterative approach described by Lin and Han [37] to find the minimum gap between the surfaces of two ellipsoids. (idea for figure from Ref. [37])

sitions  $\mathbf{y}_i^*$  and  $\mathbf{y}_j^*$  of the previous computation instead. Since particle configurations do not change much during one time step this often enables convergence within only one iteration and results in a further reduction of the average total number of iterations per gap computation from almost 40 to less than 1.01 for  $\Lambda = 1/3$ . The same result is found in typical simulations of particles with other aspect ratios  $1/4 \leq \Lambda \leq 4$ .

## B. Diverging lubrication interactions

Cox [10] and later Claey's and Brady [11] expand the surfaces of two particles  $i$  and  $j$  near contact around their closest points  $\mathbf{y}_i^*$  and  $\mathbf{y}_j^*$  as

$$x_3 = -\frac{x_1^2}{2S_1} - \frac{x_2^2}{2S_2} - \sum_{k=0}^3 \Gamma_k x_1^{3-k} x_2^k + \mathcal{O}(r^4) \quad (19)$$

and

$$x'_3 = \frac{x_1'^2}{2S_1'} + \frac{x_2'^2}{2S_2'} + \sum_{k=0}^3 \Gamma'_k x_1'^{3-k} x_2'^k + \mathcal{O}(r'^4) \quad (20)$$

in the tangential coordinates  $x_1$  and  $x_2$  that are measured along the directions of principal curvature of the respective particle, given in Eq. 14. Here and in the following, primed variables refer to the surface of particle  $j$  and unprimed ones to the one of  $i$ . The  $\Gamma_{0-3}$  are the coefficients of the third-order terms in the expansion. The error terms scale as the fourth power of the tangential distance  $r = \sqrt{x_1^2 + x_2^2}$  from the gap position. In fact, Cox [10] in general considers only the quadratic terms in Eq. 19 and Eq. 20 while Claey's and Brady [11] expand up to even fourth-order. Here, only second and third order are taken into account. The fourth-order coefficients are needed only for a weakly diverging  $\ln h$  contribution to surface-normal lubrication forces [11] which at small gaps  $h$  must be dominated by the  $h^{-1}$  term (see also appendix). As is shown in Fig. 3,  $\phi$  denotes the angle between the principal directions of curvature of both surfaces and both  $x_3$ -axes point in the direction of  $\mathbf{h}$  while the origins,  $\mathbf{y}_i^*$  and  $\mathbf{y}_j^*$ , obviously differ.

In Ref. [10] and Ref. [11], the asymptotic behavior for small  $h$  of the force  $\bar{\mathbf{F}}$  and torque  $\bar{\mathbf{T}}$  on each of the surfaces

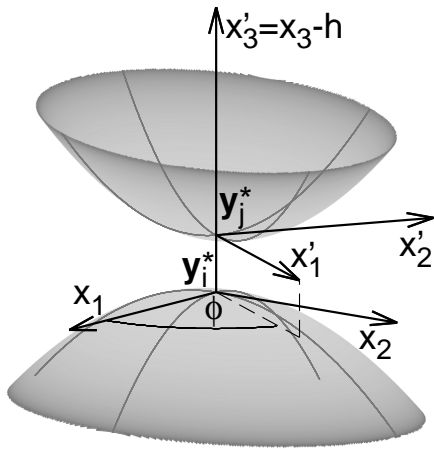


FIG. 3. The coordinate axes as defined by Cox [10] and by Claeys and Brady [11] for the approximation of the two surfaces at the minimum gap as bivariate cubic polynomials. (idea for figure from Ref. [11])

$i$  and  $j$  is analyzed in dependence of the translational and rotational velocities  $\bar{\mathbf{V}}$  and  $\bar{\boldsymbol{\Omega}}$  of both  $i$  and  $j$ . The bar on vector quantities is used to indicate a representation in the local surface coordinates  $\{x_1, x_2, x_3\}$  associated with particle  $i$ . Since the diverging terms depend only on the relative velocities, the relation can be expressed as

$$\begin{pmatrix} \bar{\mathbf{F}}_i \\ \bar{\mathbf{T}}_i \end{pmatrix} = - \begin{pmatrix} \bar{\mathbf{F}}_j \\ \bar{\mathbf{T}}_j \end{pmatrix} = \mu \mathbf{K} \begin{pmatrix} \bar{\mathbf{V}}_j - \bar{\mathbf{V}}_i \\ \bar{\boldsymbol{\Omega}}_j - \bar{\boldsymbol{\Omega}}_i \end{pmatrix} + \mathcal{O}(h^0), \quad (21)$$

with a  $6 \times 6$  resistance matrix  $\mathbf{K}$  [10, 11].  $\mathbf{K}$  is symmetric and some of the elements are zero as the corresponding forces and torques remain finite upon contact. Thus, there are only 16 independent non-zero matrix elements  $K_{\gamma\delta}$  which are functions of the gap  $h$ , the angle  $\phi$ , and the expansion coefficients in Eq. 19 and Eq. 20. These  $K_{\gamma\delta}$  can be obtained from the literature [10, 11] but are listed in the appendix for the sake of completeness. Since a part of the lubrication interactions is already accounted for by the LB method, only a correction for small gaps is required. Analogously to Ladd's initial approach in Eq. 11 [24, 27], a corrective resistance matrix  $\tilde{\mathbf{K}}$  is constructed from the differences

$$\tilde{K}_{\gamma\delta}(h) = \begin{cases} K_{\gamma\delta}(h) - K_{\gamma\delta}(\Delta_{\gamma\delta}) & \text{for } h < \Delta_{\gamma\delta} \\ 0 & \text{for } h \geq \Delta_{\gamma\delta} \end{cases} \quad (22)$$

of the diverging resistance terms at the actual gap  $h$  and at a cut-off distance  $\Delta_{\gamma\delta}$ . Following Nguyen and Ladd [27], only three independent cut-offs are used,  $\Delta_{33} \equiv \Delta_n$  for the coupling of normal translation and force,  $\Delta_{44} = \Delta_{45} = \Delta_{54} = \Delta_{55} \equiv \Delta_r$  for the coupling of angular velocities and torques, and  $\Delta_t$  for all further resistances. Suitable values have to be found empirically depending on  $\tau$  [27].

For spheroids, the quadratic coefficients  $1/(2S_1(p))$  and  $1/(2S_2(p))$  are known already from Eq. 15 where

$p$  is defined by Eq. 13 and the known surface position  $\mathbf{y}^*$ . The symmetry of the particles causes  $\Gamma_1 = \Gamma_3 = 0$ . The remaining cubic coefficients

$$\Gamma_0(p) = \frac{(R_{\parallel}^2 - R_{\perp}^2)R_{\parallel}R_{\perp} \sin p \cos p}{2s_1^6(p)} \quad (23)$$

$$\Gamma_2(p) = \frac{(R_{\parallel}^2 - R_{\perp}^2)R_{\parallel} \sin p \cos p}{2R_{\perp}s_1^4(p)} \quad (24)$$

are the result of an expansion of Eq. 13 up to third order in  $x_1$  and  $x_2$ .

The method can be applied to more complex particle shapes provided that the minimum gap, the principal curvatures, and the cubic coefficients can be determined. The extension to mixtures of particles of different shape or dimension can complicate the implementation to some extent but is no further problem if an algorithm to find the minimum separation exists, as the other parameters are properties of a single particle. The most serious limitations are the requirement of smooth surfaces that allow for a third-order expansion in every point and that the surfaces must be such that for  $h = 0$  they would touch in only one point [10]. This allows, for example, the application to one sufficiently smoothly capped cylinder interacting with a sphere but not to two such cylinders in parallel orientation side by side. The occurrence of  $\sqrt{\lambda_1\lambda_2}$  in the denominator of all matrix elements Eq. A.1 to Eq. A.16 leads to divergence if at least one of the curvature eigenvalues defined in the appendix is zero and resembles the second limitation directly. Taking the finite particle length for the maximum radius of curvature, as suggested by Butler and Shaqfeh [38], might be a viable solution to this problem. Unfortunately, the curvature of the popular spherocylinder is still discontinuous at the transition line between the cylinder and the hemispherical caps which might cause numerical difficulties.

Knowing the directions along which  $x_1$ ,  $x_2$ , and  $x_3$  are measured, the transformation of  $\bar{\mathbf{V}}_i$ ,  $\bar{\boldsymbol{\Omega}}_i$ ,  $\bar{\mathbf{F}}_i$ , and  $\bar{\mathbf{T}}_i$  to and from  $\mathbf{V}_i$ ,  $\boldsymbol{\Omega}_i$ ,  $\mathbf{F}_i$ , and  $\mathbf{T}_i$  in the particle-independent coordinate system in which the integration is carried out is straightforward to achieve. For rigid bodies the relations with the center of mass velocities  $\mathbf{v}_i$  and  $\boldsymbol{\omega}_i$  of a particle then read

$$\mathbf{V}_i = \mathbf{v}_i + \boldsymbol{\omega}_i \times (\mathbf{y}_i^* - \mathbf{r}_i) \quad (25)$$

$$\text{and } \boldsymbol{\Omega}_i = \boldsymbol{\omega}_i \quad (26)$$

and the resulting force and torque on the particle are

$$\mathbf{f}_i = \mathbf{F}_i \quad (27)$$

$$\text{and } \mathbf{t}_i = \mathbf{T}_i + (\mathbf{y}_i^* - \mathbf{r}_i) \times \mathbf{F}_i. \quad (28)$$

### C. Treatment of particle contact

In practice, the surface-normal lubrication interactions do not suffice to prevent particle contact, especially in dense systems. The lubrication interactions therefore are often reported to be clipped at a specific value to avoid

numerical instabilities [25, 32, 33, 39] and a short-range repulsive force is added to act against unphysical clustering or even overlap of particles [13, 25, 26, 29, 32, 33, 40]. To limit the forces and torques resulting from the lubrication corrections to finite values, the gap entering Eq. 22 is not allowed to be smaller than a short-range cut-off  $h_c$  independently from the actual gap  $h$ . For  $h < h_c$  a Hookean repulsive force

$$F_r(h) = \epsilon_c \begin{cases} (h_c - h) & \text{for } 0 < h < h_c \\ h_c & \text{for } h \leq 0 \end{cases} \quad (29)$$

with a stiffness  $\epsilon_c$  is applied along the  $x_3$ -direction which itself is limited to the magnitude achieved at  $h = 0$ . Effectively, this implementation of a short-range repulsion is identical to the one applied by Kromkamp *et al.* [26] who refer to Ball and Melrose [41]. Here, it is chosen solely because of its simplicity. Alternative phenomenological approaches can be found in the literature [8, 25, 33, 42]. Repulsion forces founded in elastic theory [29, 43] or even more elaborate contact descriptions [44] can be employed if the objective is to capture non-hydrodynamic interactions of particles. The complete lubrication correction and contact model reads

$$\begin{aligned} & \begin{pmatrix} \bar{\mathbf{F}}_i \\ \bar{\mathbf{T}}_i \end{pmatrix} \\ &= \begin{cases} \mu \tilde{\mathbf{K}}(h) \begin{pmatrix} \bar{\mathbf{V}}_j - \bar{\mathbf{V}}_i \\ \bar{\boldsymbol{\Omega}}_j - \bar{\boldsymbol{\Omega}}_i \end{pmatrix} & \text{for } h > h_c \\ \mu \tilde{\mathbf{K}}(h_c) \begin{pmatrix} \bar{\mathbf{V}}_j - \bar{\mathbf{V}}_i \\ \bar{\boldsymbol{\Omega}}_j - \bar{\boldsymbol{\Omega}}_i \end{pmatrix} - F_r(h) \hat{\mathbf{E}}_3 & \text{for } h \leq h_c \end{cases} \\ &= - \begin{pmatrix} \bar{\mathbf{F}}_j \\ \bar{\mathbf{T}}_j \end{pmatrix}, \end{aligned} \quad (30)$$

with  $\hat{\mathbf{E}}_3$  being the unit 6-vector connected with the  $x_3$ -direction of the force  $\mathbf{F}_i$ .

The above treatment introduces two additional parameters  $h_c$  and  $\epsilon_c$ . When modeling a physical suspension, it can be interpreted as modeling ‘‘residual Brownian forces or particle roughness’’ [40] and the parameters can be used to control the strength of non-hydrodynamic effects. When targeting the theoretical model system of smooth particles in the absence of Brownian motion, care must be taken to ensure that the influence of the non-hydrodynamic contact modeling is sufficiently small to be neglected. Then the results of a simulation do not depend on the exact values of the parameters  $h_c$  and  $\epsilon_c$ . Since in this view,  $h_c$  and  $\epsilon_c$  are purely numerical parameters they should not be rescaled as physical quantities when a simulation is transformed from one spatial resolution to another. Instead it appears reasonable to keep  $h_c$  constant when measured in lattice units so the lubrication corrections are applied down to smaller relative gaps  $h/R$  at higher resolution  $R$ . From Eq. 29 it is easily seen that the maximum repulsive force is  $\epsilon_c h_c$ . In order to prevent particle overlap it should scale as the viscous forces, estimated as  $6\pi\mu R^2\dot{\gamma}$  for flows with a shear rate  $\dot{\gamma}$  [13, 40]. Since in this work  $\tau = 1$  is assumed, a transformation from one resolution to another

does not change the viscosities and also  $R^2\dot{\gamma}$  must stay constant as it is proportional to the particle Reynolds number  $\text{Re}_p = 4R^2\dot{\gamma}/\nu$ . Thus  $\epsilon_c$  should be kept constant then as well.

Also the present implementation of a link-based lubrication model as in Eq. 12 employs a, then link-wise, clipping of the lubrication force equivalent to the one in Eq. 30 and a short-range repulsive force with a functional dependency on the gap width identical to Eq. 29. Since in this case the gap is measured link-wise and the force is not applied once per particle along the surface-normal direction but once per link along the link direction, separate values for the now link-wise parameters  $\epsilon_c^*$  and  $h_c^*$  are required in general. The link-wise correction forces further correspond to stresses, therefore  $\epsilon_c^* h_c^*$  should scale as  $6\pi\mu\dot{\gamma}$  [33] to prevent overlap and  $\epsilon_c^*$  requires appropriate rescaling upon changing the resolution if  $h_c^*$  is kept constant.

#### IV. VALIDATION AND COMPARISON TO OTHER MODELS

##### A. Pair interactions of spheres

For spheres, the lubrication corrections developed here are equivalent to the ones of Nguyen and Ladd [27] who, however, present detailed validation only for the interaction of a single sphere and a planar wall. The accuracy of the present method is studied for the more frequent interaction of two identical spheres. This setup is particularly suited for validation since good analytical approximations exist [45]. For their link-wise model, Ding and Aidun [31] show only the normal force between spheres plotted on a linear scale which makes it hard to appreciate the actual accuracy of the method, while the analysis of Clausen [33] is performed for a resolution of the particle radius with  $R = 10$  lattice sites that for non-deformable particles seems unnecessarily large. Therefore, also a comparison with the link-wise model at different  $R$  follows.

In all tests one particle is placed with a random offset with respect to the lattice near the center of a closed cubic box which imposes a no-slip condition on the fluid velocity. In a preliminary study, the size of the box is chosen to be  $15R$  as a viable compromise between computational costs and the undesired enhancement of the single-particle resistances by interaction with the wall which decays only slowly with increasing box size. Another particle is placed at a random position with a prescribed gap  $h$  between both surfaces. For simplicity, the direction from the first to the second particle is referred to as  $w_3$  and two further directions  $w_1$  and  $w_2$  are chosen randomly but mutually orthogonal to form a right-handed system. While the first particle is held fixed, the second particle is forced to either translate with a constant velocity  $v$  along  $w_1$  or  $w_3$  or to rotate with an angular velocity  $\omega$  about  $w_1$ . The magnitude of the ve-

locities is chosen to result in a fixed Reynolds number  $Re = vR/\nu = \omega R^2/\nu = 6 \times 10^{-8}$  with  $\nu = 1/6$  for all  $R$ . As was tested by increasing  $Re$  by a factor of 10, no inertial effects are visible. The simulations are allowed to run for several  $10^3$  LB steps until a steady state is reached. The motion of the particle during this time is negligible and no changes in the discretization are observed in general. Apart from effects of discretization and confinement which are not expected to diverge for decreasing  $h$ , symmetry arguments dictate that a translation along  $w_1$  and  $w_3$  results in a force in the respective opposite direction, a rotation about  $w_1$  results in a torque in the opposite direction, and additionally, translation and rotation along  $w_1$  results in a torque about  $w_2$  and a force along  $-w_2$ , respectively. For each  $R$ , the magnitude of these forces and torques is averaged over at least 15 random configurations with the same value of  $h$ . Since the particle motion is prescribed, there is no need for a short-range lubrication cut-off and repulsion, thus  $h_c = \epsilon_c = 0$  is set. From comparison with the results by Jeffrey and Onishi [45] suitable long-range cut-offs at  $\tau = 1$  for all  $R$  are found to be

$$\Delta_n = \frac{2}{3}, \quad \Delta_t = \frac{1}{2}, \quad \text{and} \quad \Delta_r = \frac{1}{4}. \quad (31)$$

The relation to the cut-offs  $h_N$ ,  $h_T$ , and  $h_R$  suggested by Nguyen and Ladd [27] is not surprising:  $\Delta_n = h_N$  and  $\Delta_t = h_T$  but  $\Delta_r \neq h_R$  because the cut-offs in Ref. [27] relate to the resistance functions of the spheres themselves while the cut-offs here relate to the resistances of the surfaces at the gap. Thus, in the lubrication correction of the torque experienced due to rotation about  $w_1$ , both  $\Delta_t$  and  $\Delta_r$  are involved while in Ref. [27] it is only  $h_R$ .

Fig. 4 displays the resistance functions related to the particle motions explained above at resolutions  $R = 2, 4$ , and 8 resulting from the choice of lubrication cut-offs given in Eq. 31. The striking similarity of Fig. 4(c) and (d) can be explained by the Lorentz reciprocal theorem [46]. The data in Fig. 4(b) and (c), and the data in (d) and (e) are taken from the same simulations. Generally, an offset with respect to the solution by Jeffrey and Onishi [45] is observed which in each figure is roughly constant for a given  $R$ . These offsets can be attributed to two effects: the analytical solution considers two particles in an infinite volume of fluid while the simulations are performed within a finite box. The interactions with the walls lead to an enhancement of the single-particle resistances, best seen in Fig. 4(b) for large  $h/R$ . Second, the effective hydrodynamic radii of particles modeled by the momentum exchange method are known to differ from the input radii  $R$ , especially at small  $R$ , which explains the more or less severe underestimation of all resistances for  $R = 2$ . The comparably large statistical errors in the data for the smallest radius must be attributed to discretization effects. All these observations could be made for single particles as well and it is not within the scope of lubrication corrections to alleviate the shortcomings but only to produce a smooth increase of the resistances

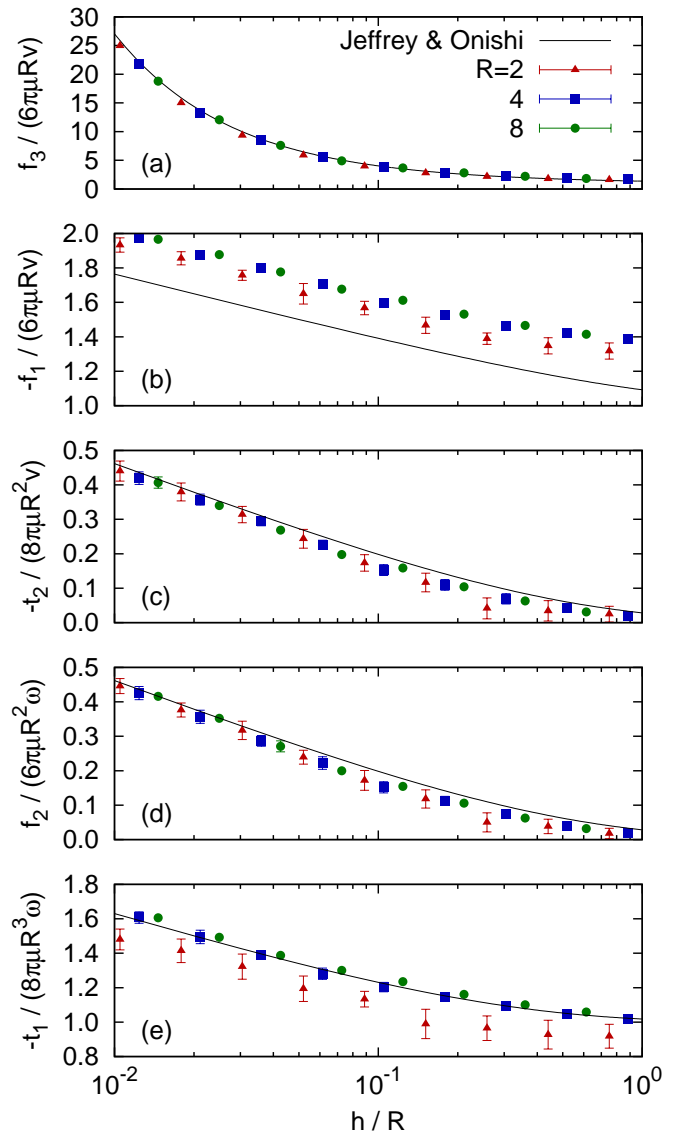


FIG. 4. (Color online) Non-dimensional resistances for one of two identical spheres of radius  $R$  aligned along direction  $w_3$  at a normalized gap  $h/R$ . Compared are simulations with the contact-based lubrication model at different resolutions of  $R$  in lattice units (symbols) with the series developed by Jeffrey and Onishi [45] (lines). (a) shows the force along  $w_3$  due to a translation with velocity  $v$  in the opposite direction, (b) the force in the perpendicular direction  $-x_1$  due to a translation along  $w_1$ , (c) the torque about  $w_2$  due to the same translation, (d) the force along  $-x_2$  due to a rotation about  $w_1$  with angular velocity  $\omega$ , and (e) the resulting torque about  $-x_1$ . Error bars quantify the standard deviation obtained from at least 15 random configurations and are drawn only where larger than the symbol itself.

with decreasing separation parallel to the theoretical solution. The lubrication model achieves this objective to very good accuracy at  $R = 4$  and 8 and, taking into account the larger discretization errors, even at  $R = 2$ .

As expected from the work of Clausen [33], the link-

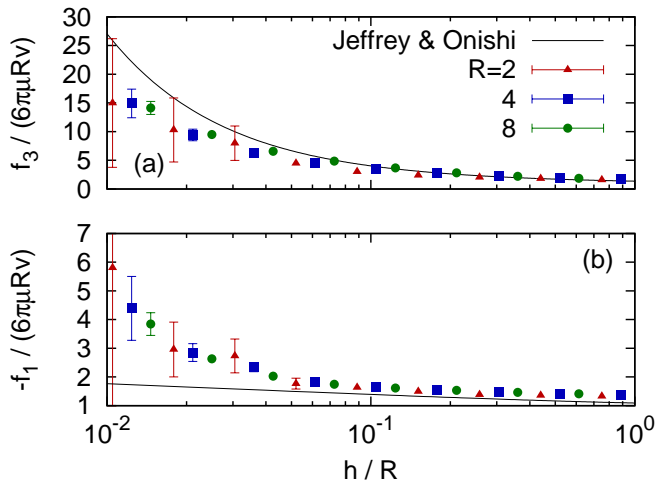


FIG. 5. (Color online) Normalized resistances as in Fig. 4 obtained from simulations with link-based lubrication corrections. For brevity, only the force due to a (a) normal or (b) tangential translation is shown, the other singular resistances appear to be qualitatively similar to case (b).

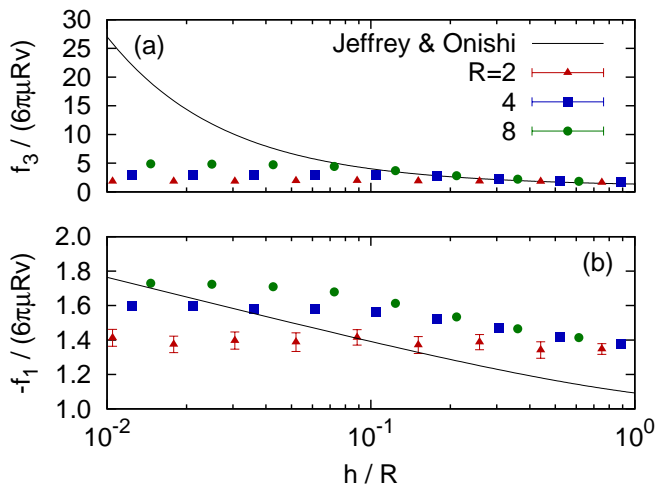


FIG. 6. (Color online) Normalized resistances as in Fig. 5 obtained from simulations without lubrication corrections.

wise model leads to an under-prediction of the normal force  $f_3$  as displayed in Fig. 5(a) while the divergence of the tangential force  $f_1$  in Fig. 5(b) is clearly over-predicted. The other non-normal singular forces and torques  $t_2$ ,  $f_2$ , and  $t_1$  are over-estimated in a qualitatively similar way at small separations. A special treatment of short-range contacts is disabled in these simulations by setting  $h_c^* = \epsilon_c^* = 0$ . Since the link-based model relies on discrete lattice links to compute lubrication corrections, severe noise is caused by an amplification of discretization errors at small distances. This effect is strongest for  $R = 2$  but visible also by the error bars obtained for the higher resolutions in Fig. 5. Finally, Fig. 6 shows the resistances to normal and tangential translation without

lubrication corrections. Again, the other non-normal resistances appear to be qualitatively similar to Fig. 6(b). It is clear that, without lubrication modeling, the singular behavior is captured only partially depending on the lattice resolution. In the case of  $R = 2$ , an increase is hardly visible for gaps  $h/R < 1$ . In Clausen's modified link-based model [33] the under-prediction of  $f_3$  appears to be reduced while all non-normal resistances remain uncorrected. At best, this model can perform as the theoretical solution for  $f_3$ , which is, as can be seen in Fig. 4(a), closely approximated by the contact-based method, and comparable to Fig. 6(b) for all other terms. The importance of non-normal interactions in dynamic simulations of many particles remains to be examined below.

## B. Pair interactions of spheroids

To validate the lubrication corrections in the case of spheroidal particles, an equivalent procedure as for spheres is followed. The long-range cut-offs in Eq. 31 found suitable for spheres are kept. Different from the case of spheres, the validation is performed not focusing on the particles as a whole but on the surfaces around the points of closest approach  $\mathbf{y}_i^*$  and  $\mathbf{y}_j^*$  on both spheroids. Thus, the coordinate system  $\{x_1, x_2, x_3\}$  is chosen as defined in Eq. 19 according to the local directions of principal curvature and the local normal direction of the first particle. While the second particle is held fixed, the first one is forced to translate and rotate in a way that causes its surface to either translate along or rotate about one of the coordinate axes and the resulting force and the torque with respect to  $\mathbf{y}_i^*$  is recorded in the same frame. Compared to spheres, the parameter space is considerably increased as a configuration is defined not only by the surface separation but also by the particle aspect ratio and the relative orientation. The purpose here lies mainly in demonstrating the physical correctness and the degree of resolution independence achievable with the presented model. For this purpose it is sufficient to exemplarily examine one fixed particle configuration at varying distances for each diverging element of  $\mathbf{K}$ . The 16 singular  $K_{\gamma\delta}$  can be reduced to the only 10 physically different cases that are displayed in Fig. 7: (a) tangential force  $K_{11}$  (equivalent to  $K_{22}$ ), (b) perpendicular tangential force  $K_{21}$ , (c) normal force  $K_{31}$  (equivalent to  $K_{32}$ ), (d) tangential torque  $K_{41}$  (equivalent to  $K_{52}$ ), and (e) perpendicular tangential torque  $K_{51}$  (equivalent to  $K_{42}$ ) due to tangential translation; (f) normal force  $K_{33}$ , (g) tangential torque  $K_{43}$  (equivalent to  $K_{53}$ ), and (h) normal torque  $K_{63}$  due to normal translation; and (i) tangential torque  $K_{44}$  (equivalent to  $K_{55}$ ) and (j) perpendicular tangential torque  $K_{54}$  due to tangential rotation. Fig. 7(a) to (e) are generated from the same set of simulations. The same is done for plots (f) and (g) and for (i) and (j). For (h)  $K_{63}$  a configuration of two prolate spheroids with aspect ratio  $\Lambda = 3$  is chosen where the axes of both

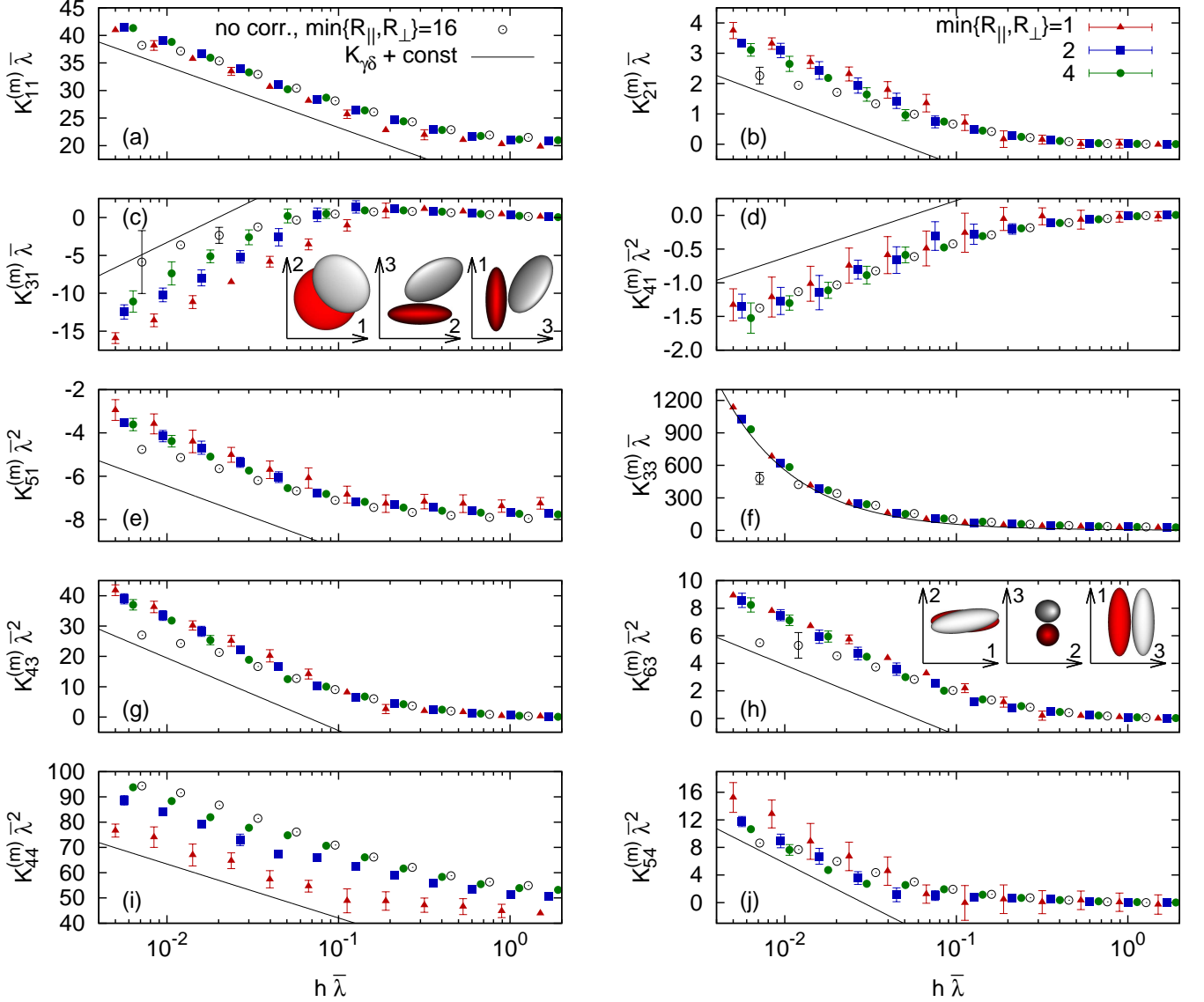


FIG. 7. (Color online) The measured resistances  $K_{\gamma\delta}^{(m)}$  for the ten independent and physically different singular types of lubrication interactions as function of the surface separation  $h$ : (a) tangential force, (b) perpendicular tangential force, (c) normal force, (d) tangential torque, and (e) perpendicular tangential torque due to tangential translation; (f) normal force, (g) tangential torque, and (h) normal torque due to normal translation; and (i) tangential torque and (j) perpendicular tangential torque due to tangential rotation. All data is obtained from the same configuration of oblate spheroids with aspect ratio  $\Lambda = 1/3$  except for (h) where prolates with  $\Lambda = 3$  are used. The two configurations are visualized in the insets of figures (c) and (h) as seen from the respective local  $x_3$ -,  $x_1$ -, and  $x_2$ -direction of the first of the two particles (drawn red, with center at lower coordinate position). Symbols refer to different resolutions of the smaller half-axis, lines to the respective correction term, shifted by an arbitrary constant. Resolutions 1 to 4 feature lubrication corrections, resolution 16 does not for comparison. The combined mean curvature  $\bar{\lambda}$  serves for non-dimensionalization.

particles are both perpendicular to the line between their centers but twisted against each other by an angle of  $10^\circ$ . The remaining resistances are examined for a randomly generated configuration of two oblates  $\Lambda = 1/3$  that results in a clear divergence of all elements but  $K_{63}$  and that is defined by the angles  $\angle(\mathbf{y}_i^* - \mathbf{r}_i, \hat{\mathbf{o}}_i) = 177.06^\circ$ ,  $\angle(\mathbf{y}_j^* - \mathbf{r}_j, \hat{\mathbf{o}}_j) = 82.591^\circ$ , and  $\angle(\hat{\mathbf{o}}_i, \hat{\mathbf{o}}_j) = 40.277^\circ$  with the respective axes of rotational symmetry  $\hat{\mathbf{o}}_i$  and  $\hat{\mathbf{o}}_j$  of

the particles. The configurations are visualized as insets of Fig. 7(c) and (h). The surface separation  $h$  but also the resistances  $K_{\gamma\delta}$  are made dimensionless using the combined mean curvature of both surfaces [11]

$$\bar{\lambda} = \frac{1}{4} \left[ \frac{1}{S_1} + \frac{1}{S_2} + \frac{1}{S'_1} + \frac{1}{S'_2} \right]. \quad (32)$$

Again the magnitude of the velocity is chosen such that  $Re$  remains constant when changing the resolution. In case of the lowest resolution  $\min\{R_{\parallel}, R_{\perp}\} = 1$  it is  $v = 10^{-8}$ . The size of the cubic simulation volume in this case is  $30 \min\{R_{\parallel}, R_{\perp}\} = 10 \max\{R_{\parallel}, R_{\perp}\} = 30$  and is scaled according to the particle resolution. For the data at resolutions 1, 2, and 4, each symbol stands for the average of at least 15 independent simulations at identical relative particle separation and orientation but a random sub-grid offset and rotation with respect to the fluid lattice. The error bars represent the standard deviations.

In the absence of theoretical results, simulations with lubrication corrections at several resolutions are compared to simulations without corrections but with a considerably increased lattice resolution  $\min\{R_{\parallel}, R_{\perp}\} = 16$  where lubrication interactions can be expected to be captured by the LB method itself already to a large extent. For these more expensive high-resolution simulations, each symbol in Fig. 7 corresponds to only 4 independent samples. Additionally, the divergence behavior expected from Eq. A.1 to Eq. A.16 is plotted with an arbitrary offset. As a further confirmation for the correct implementation of the method, Newton's third law in Eq. 30 is not exploited to save computations but the effects on both surfaces are computed independently and checked for consistency. Indeed, the forces and torques are found to be equal but opposite apart from small deviations attributed to the error in the anti-parallelism of the normal directions of both surfaces according to Eq. 18.

In Fig. 7 the resistances obtained with lubrication corrections at the larger resolutions  $\min\{R_{\parallel}, R_{\perp}\} = 2$  and 4 appear largely parallel to each other and consistent with data from the uncorrected simulations at resolution 16. Of course, also at this highest resolution the lubrication interactions as resolved by the LB method alone eventually break down at the smallest separations and consequentially depend strongly on the discretization of the gap. These effects are best visible in Fig. 7(h) and (c). Still, at least for intermediate gaps, the resistances obtained at resolution 16 are well compatible with the theoretical divergence terms  $K_{\gamma\delta}$ . Simulations at the lowest resolution  $\min\{R_{\parallel}, R_{\perp}\} = 1$  tend to suffer more from discretization errors and in general feature a less smooth transition from the non-singular long-range behavior to the short-range regime that is dominated by the  $K_{\gamma\delta}$ . For the chosen particle configuration, the normal force induced by a tangential translation, displayed in Fig. 7(c), seems to be particularly difficult to capture properly: for large gaps the resistance seems identical at all resolutions but in the region where lubrication interactions dominate an offset is visible not only at resolution 1 but also between resolutions 2 and 4, and compared to resolution 16 without corrections. This indicates that in this particular case, different than assumed, the divergence of  $K_{31}$  is not resolved by the LB method down to a separation of approximately one lattice unit. A possible explanation lies in the fact that  $K_{31}$  (given in Eq. A.3)

depends on the third order coefficients  $\Gamma_0$  and  $\Gamma_2$  of both particles. On the second particle,  $\mathbf{y}_j^*$  lies near the edge (see inset of Fig. 7(c)) where according to Eq. 15 the minimum radius of curvature for an oblate of aspect ratio 1/3 is only  $R_{\parallel}/3$ . Even at resolution 4, the radius is only 4/3 and the third-order features of the surface cannot be expected to be resolved well at this resolution. It is not clear why equivalent difficulties do not exist for the normal force induced by a tangential rotation depicted in Fig. 7(g) that also depends on  $\Gamma_0$  and  $\Gamma_2$  in the same configuration of particles. The error bars, also of the data at resolution 16 without corrections, suggest that  $K_{31}$  in this configuration is particularly susceptible to discretization effects. Nevertheless, at resolution  $\min\{R_{\parallel}, R_{\perp}\} = 2$  the offset to higher resolution data at small gaps does not appear exceedingly large as compared to the results for the other resistances. In the following simulations of spheroidal particles a length of the smaller half-axis of 2 lattice units is regarded as minimum spatial resolution.

### C. Many particles in suspension: shear-induced diffusion and viscosity

The initialization of densely-packed configurations of many particles without overlap is not trivial already for spherical particles. A growth method similar to the ones described in the literature [3, 47] is applied: the particles are initially scaled down to typically only 30% of their linear size, so an overlap-free placement at random positions is easily achieved. The half-axes are then slowly grown to their actual size. During the growth, the particles are free to reorient and move but lubrication and hydrodynamic interactions are replaced by simple damping terms for the velocities and only the Hookean short-range repulsion defined in Eq. 29 is acting. Growing the particles to dimensions slightly beyond their final size and resetting the size afterwards assures a certain minimum separation in the generated particle configuration.

As a first benchmark, the shear-induced self-diffusion of spherical particles in the direction of a velocity gradient is studied. Accurate data for supposedly purely hydrodynamically interacting spheres in Stokes flow is reported by Sierou and Brady [40]. Lees-Edwards boundary conditions [48] impose a well-defined shear rate in an otherwise periodic system with cubic dimensions to mimic an infinite volume of fluid. Depending on the volume fraction  $\Phi$ , between 800 to 4000 particles are modeled, which, according to Ref. [40] should allow for sufficiently reliable results. In the case of a resolution of  $R = 4$ , the simulation comprises  $128^3$  lattice sites. Initially, all systems are equilibrated with the shear for a time interval of roughly  $130\dot{\gamma}^{-1}$ . For each particle  $i$ , the trajectory  $x_i(t)$  in velocity gradient direction is recorded during another  $630\dot{\gamma}^{-1}$  and the mean-square displacement  $\langle \Delta x^2(\Delta t) \rangle = \langle (x_i(t+\Delta t) - x_i(t))^2 \rangle_{i,t}$  during a time interval  $\Delta t$  is computed as an average over all particles  $i$  and starting times  $t$ .

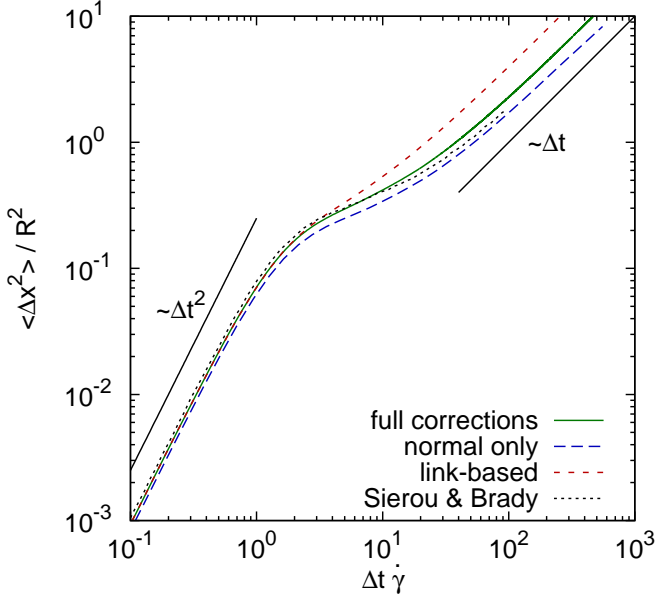


FIG. 8. (Color online) Shear-induced self-diffusion in suspensions of spheres with radius  $R = 4$  as obtained with the full contact-based corrections, the same with non-normal corrections disabled, and the link-based approach. The mean square displacement in velocity gradient direction at a solid volume fraction of  $\Phi = 0.2$  is shown. Results from accelerated Stokesian dynamics simulations by Sierou and Brady [40] are plotted for comparison.

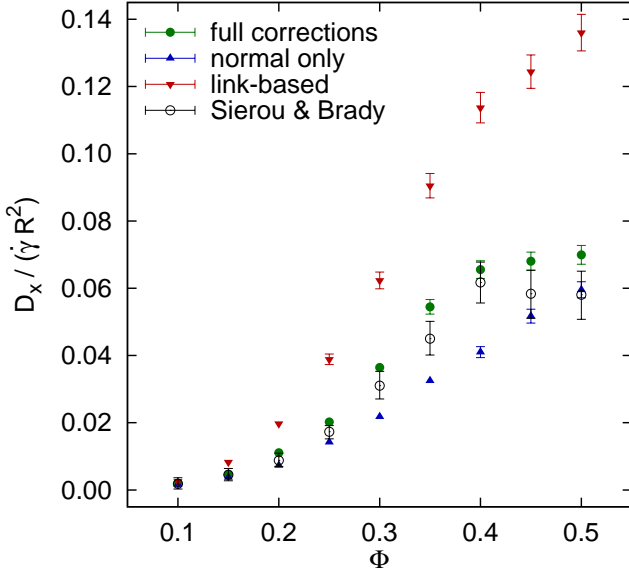


FIG. 9. (Color online) Shear-induced self-diffusion as in Fig. 8. The diffusion coefficients in velocity gradient direction computed from the mean-square displacement as shown in Fig. 8 are displayed as a function of the volume fraction  $\Phi$ . Results from accelerated Stokesian dynamics simulations by Sierou and Brady [40] are shown for comparison. The error bars represent an estimated statistical error of 4% and are drawn only where larger than the corresponding symbol.

Fig. 8 compares the mean-square particle displacement  $\langle \Delta x^2 \rangle$  for  $\Phi = 0.2$  as a function of the time interval  $\Delta t$  as obtained from the contact-based method presented above, the link-wise method briefly sketched in section II, and the contact-based method with all non-normal lubrication corrections disabled with the results by Sierou and Brady [40]. As expected, over short times  $\Delta t$  the particle velocities are self-correlated and a scaling  $\langle \Delta x^2 \rangle \sim \Delta t^2$  is found. For large  $\Delta t$  hydrodynamic interactions lead to decorrelation and the relation becomes diffusive with  $\langle \Delta x^2 \rangle \sim \Delta t$ . All lubrication corrections capture the short-time behavior consistently and show diffusion at long times. While, however, in the two contact-based simulations, the magnitude of the diffusion is only moderately under- and over-predicted as compared to the literature, the link-wise corrections lead to a considerable over-prediction by roughly 100%. This observation is made for the full range of volume fractions when comparing the resulting diffusion coefficients  $D_x$ , obtained for large  $\Delta t$  from fits  $\langle \Delta x^2 \rangle = 2D_x\Delta t + \text{const}$ , as it is done in Fig. 9. By repeating the simulations using four different random starting configurations for  $\Phi = 0.2$  and  $0.4$ , the statistical errors are estimated to be  $\Delta D_x = 0.0004$  and  $0.002$ , respectively, or 4% and 2% of the respective  $D_x$  itself. In Fig. 9, a relative statistical error of 4% is assumed for all data. In the case where the non-normal interactions are disabled,  $D_x$  continues to grow as a function of  $\Phi$  at  $\Phi > 40\%$  where all other datasets show a plateau or at least a significantly reduced slope. In general, the full contact-based corrections are most consistent with literature data. The remaining discrepancy might be caused by finite size effects or by small deviations in the effective hydrodynamic particle radii. The finite particle Reynolds number  $Re_p = 4R^2\dot{\gamma}/\nu = 0.24$  seems sufficiently small to justify the comparison with Stokesian dynamics simulations. In their recent publication [7], Yeo and Maxey, using the lubrication-corrected force coupling method, find values of  $D_x$  almost identical to those in Ref. [40] even at (according to the above definition)  $Re_p = 0.4$ .

Obviously, the influence of the free short-range parameters  $h_c^{(*)}$  and  $\epsilon_c^{(*)}$  on shear-induced diffusion needs to be examined. In the present simulations,  $h_c = 0.01$  and  $\epsilon_c = 100$  is chosen for the two contact-based cases and  $h_c^* = 0.04$  and  $\epsilon_c^* = 100$  for the link-wise corrections. Measured on the scale of viscous forces or stresses, this corresponds to maximum repulsions of  $h_c\epsilon_c/(6\pi\mu R^2\dot{\gamma}) \approx 30$  and  $h_c^*\epsilon_c^*/(6\pi\mu\dot{\gamma}) \approx 2000$ , respectively. In Tab. I, diffusion coefficients for volume fractions  $\Phi = 0.2$  and  $0.4$  are shown at varying  $h_c$  and  $\epsilon_c$  for different lubrication models at resolution  $R = 4$ . Additionally, data for resolutions  $R = 2$  and  $8$  is shown where  $h_c$  and  $h_c^*$  are kept fixed and  $\epsilon_c$  and  $\epsilon_c^*$  are chosen such that the respective dimensionless maximum repulsion is the same as for  $R = 4$ . The numbers do not seem very sensitive to even large changes in the short-range parameters of  $h_c$  to 50 or 1000 and of  $\epsilon_c$  to 0.1 or 0.001, the largest relative change being a reduction of about 12% at  $\Phi = 0.4$  for  $h_c = 0.1$ .

$h_c^{(*)}$	$\epsilon_c^{(*)}$	model	$R$	$D_x(\Phi=0.2)$	$D_x(\Phi=0.4)$
0.01	100	full	4	$0.011 \pm 0.0004$	$0.066 \pm 0.002$
0.1	100	full	4	0.012	0.058
0.001	100	full	4	0.010	0.068
0.01	50	full	4	0.011	0.064
0.01	1000	full	4	0.011	0.063
0.01	100	normal only	4	0.0073	0.041
0.04	100	link-based	4	0.020	0.11
0.01	100	full	2	0.011	0.062
0.01	100	normal only	2	0.0070	0.035
0.04	400	link-based	2	0.021	0.10
0.01	100	full	8	0.011	0.068
0.01	100	normal only	8	0.0085	0.050
0.04	25	link-based	8	0.019	0.14

TABLE I. Shear-induced self-diffusion  $D_x$  in the velocity-gradient direction for spherical particles at volume fractions  $\Phi = 0.2$  and  $0.4$  using different lubrication models, resolutions  $R$ , and short-range numerical parameters  $h_c$  and  $\epsilon_c$  ( $h_c^*$  and  $\epsilon_c^*$  in case of link-based lubrication corrections). The particle Reynolds number is  $\text{Re}_p = 4R^2\dot{\gamma}/\nu = 0.24$ . Statistical error estimates are computed from simulations with different random seeds for  $h_c = 0.01$ ,  $\epsilon_c = 100$ , and  $R = 4$  exemplarily.

Interestingly, the same change effects an increase of  $D_x$  at  $\Phi = 0.2$ . Values  $\epsilon_c < 50$  do not suffice to prevent particles from overlapping in the present simulations. It is surprising that for  $\Phi = 0.2$ , diffusion remains unchanged when reducing the resolution to only  $R = 2$  or doubling it to  $R = 8$  and also at  $\Phi = 0.4$  there hardly is a significant dependency on  $R$ . It appears that shear-induced self-diffusion at the volume fractions considered is determined rather by short-range lubrication interactions than by hydrodynamic interactions acting over larger length scales that could be resolved by pure LB simulations at practical resolutions of the particle radii. The results for purely normal and link-wise lubrication corrections remain qualitatively unchanged when varying the resolution: without non-normal corrections, diffusion is reduced by 23 to 44 %, the link-wise model leads to an increase between 61 and 106 %, depending on resolution and volume fraction. Unlike the full model, the two other methods show a significant dependency on the resolution except for the link-based model at  $\Phi = 0.2$ .

There seems to be less freedom in the choice of the short range parameters  $h_c^*$  and  $\epsilon_c^*$  associated with the link-based lubrication model than for the contact-based model. Significant deviations from the combination  $h_c^* = 0.04$  and  $\epsilon_c^* = 100$  at  $R = 4$  are often found to lead to numerical instabilities even when the time step for the particle update is reduced. Still, the over-estimation of diffusion by the link-wise model is too strong to be attributed solely to the treatment of particle contacts. The stability problems might be caused by the relatively large discretization errors of the method that are visible

in Fig. 5. A related issue consists in contacts with large curvatures of the involved particle surfaces staying undetected due to an insufficient resolution of the surfaces by lattice links. In consequence, unphysically close approach or even overlap of particles is possible. If the discretization changes because the involved particles are moving with respect to the lattice, the contact can get resolved and large repulsive forces and changes in the particles' resistances can emerge suddenly. Though such events are rare and thus are not expected to affect the observables in a large system they can cause a simulation to crash. At large particle resolutions, as chosen by Clausen [33], this problem is less likely to occur.

As a second benchmark, the shear viscosity of suspensions is considered. For viscosity computation, the method successfully applied before [30] is used: different from the full Lees-Edwards boundary conditions employed above, the particles are now prevented from crossing the sheared boundaries at which the shear stress  $\sigma$  is computed. To exclude boundary effects, the shear rate  $\dot{\gamma}$  and the actual particle volume fraction  $\Phi$  are computed only from the particles in the central half of the system. Depending on the volume fraction and particle aspect ratio, the total simulations comprise between about 600 and 9000 particles which is more than sufficient to obtain reliable results [42]. At the beginning of a simulation, each system is allowed a time of the order of  $20\dot{\gamma}^{-1}$  for equilibration. An equally long consecutive interval of time is used for data accumulation. The statistical errors are estimated from the fluctuations of  $\dot{\gamma}$  and  $\sigma$  over time that are propagated into the relative suspension viscosity  $\mu_r = (\sigma/\dot{\gamma})/\mu$ .

The viscosities thus obtained are plotted as a function of  $\Phi$  in Fig. 10(a) in the case of spheres. The resolution is  $R = 4$  and again the three different lubrication models are compared: the contact-based model developed above, the link-based model briefly sketched in section II, and the contact-based model with all non-normal corrections disabled. Of these three cases, the full contact-based model clearly shows the best consistency with the accelerated Stokesian dynamics simulations by Sierou and Brady [42] and the simpler method by Bertevas *et al.* [13] that both similarly aim at the simulation of purely hydrodynamically interacting particles at low Reynolds number shear flow. While the link-wise model leads to an over-prediction of viscosities, the omission of non-normal corrections results in erroneously low viscosities. In view of Fig. 5(b) and Fig. 6(b) it seems plausible to attribute these errors directly to the over- or under-prediction of non-normal lubrication interactions. The similarity of the data for purely normal lubrication corrections as compared with the results by Hyväluoma *et al.* [25] obtained at a somewhat higher resolution of  $R = 6$  using normal lubrication corrections of the type of Eq. 11 confirms the validity of the LB implementation and of the procedure for viscosity measurement employed here. It is interesting that for  $\Phi \lesssim 0.2$  all three lubrication models produce viscosities that are hard to

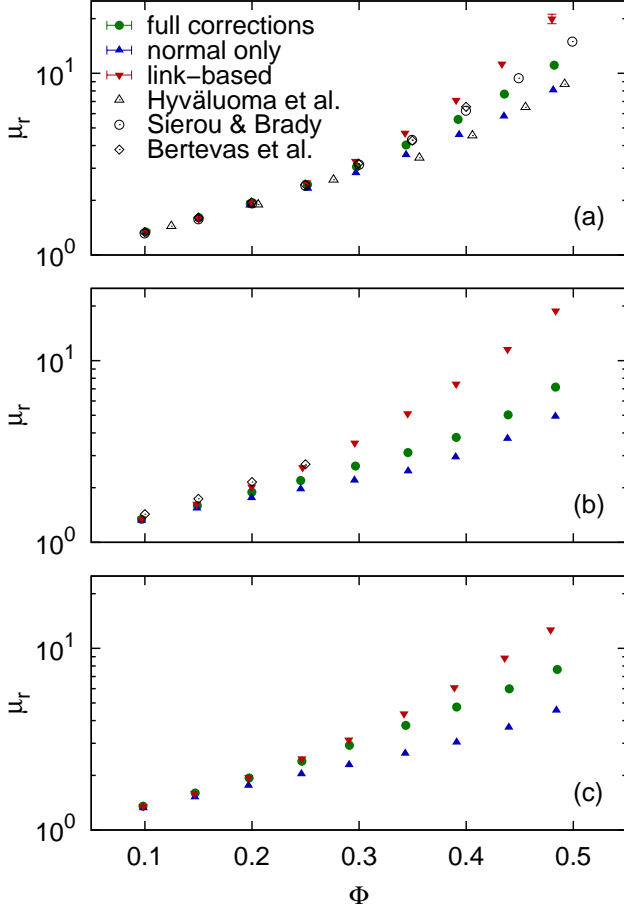


FIG. 10. (Color online) Relative suspension viscosity  $\mu_r$  in dependence on the solid volume fraction  $\Phi$  as obtained with the full contact-based corrections, the same with non-normal corrections disabled, and the link-based approach for (a) spheres with radius  $R = 4$ , (b) oblates with  $R_{\parallel} = 2$ ,  $R_{\perp} = 6$  (aspect ratio  $\Lambda = 1/3$ ), and (c) prolates with  $R_{\parallel} = 6$ ,  $R_{\perp} = 2$  ( $\Lambda = 3$ ). For spheres, data is compared with results from LB simulations with only normal corrections at  $R = 6$  by Hyväluoma *et al.* [25], accelerated Stokesian dynamics simulations by Sierou and Brady [42] and the method by Bertevas *et al.* [13]. Also for oblates, data for the least aspherical aspect ratio  $\Lambda = 0.3$  studied by Bertevas *et al.* [13] is shown. Error bars for original data are drawn only where larger than the corresponding symbol.

distinguish, even on the logarithmic scale of  $\mu_r$  in the figure. Apparently, lubrication interactions, at least the non-normal ones, contribute only weakly to the viscosity at these volume fractions.

Tab. II compares the viscosities resulting from a variation of the short-range parameters for  $\Phi = 0.5$  where the effect of lubrication interactions is strongest. Apparently, varying  $\epsilon_c$  has no significant effect on the resulting viscosities. Better resolving lubrication interactions by reducing  $h_c$  to only 0.001 leads to an increase of  $\mu_r$  that is noticeable but still smaller than 10%. Reducing the resolution of lubrication corrections, however, by choos-

$h_c^{(*)}$	$\epsilon_c^{(*)}$	model	$R$	$\Phi$ [ $10^{-2}$ ]	$Re_p$	$\mu_r$
0.01	100	full	4	$48.2 \pm 0.9$	0.14	$11.1 \pm 0.3$
0.1	100	full	4	$48 \pm 3$	0.15	$8.9 \pm 0.3$
0.001	100	full	4	$48.2 \pm 0.8$	0.13	$11.8 \pm 0.3$
0.01	50	full	4	$48.2 \pm 0.7$	0.14	$10.9 \pm 0.3$
0.01	1000	full	4	$48 \pm 1$	0.14	$10.9 \pm 0.4$
0.01	100	normal only	4	$48 \pm 1$	0.16	$8.1 \pm 0.2$
0.04	100	link-based	4	$48.0 \pm 0.4$	0.10	$20 \pm 1$
0.01	100	full	2	$48 \pm 1$	0.15	$8.8 \pm 0.4$
0.01	100	normal only	2	$48 \pm 3$	0.17	$5.9 \pm 0.2$
0.04	400	link-based	2	$46.4 \pm 0.5$	0.16	$9.9 \pm 0.6$
0.01	100	full	8	$48.4 \pm 0.7$	0.13	$12.4 \pm 0.2$
0.01	100	normal only	8	$48.3 \pm 0.9$	0.14	$9.6 \pm 0.2$
0.04	25	link-based	8	$48.0 \pm 0.6$	0.08	$28 \pm 1$

TABLE II. Relative shear viscosity  $\mu_r$  of dense ( $\Phi \approx 0.5$ ) suspensions of spherical particles for different lubrication models, resolutions  $R$ , and short-range numerical parameters  $h_c$  and  $\epsilon_c$  ( $h_c^*$  and  $\epsilon_c^*$  in case of link-based lubrication corrections). The effective volume fraction  $\Phi$  and particle Reynolds number  $Re_p = 4R^2\dot{\gamma}/\nu$  vary slightly due to the simulation setup.

ing  $h_c = 0.1$  causes a reduction of the viscosity by 20% to a value that is actually closer to data without non-normal corrections than to data from the full model at  $h_c = 0.01$ . Variations in the volume fraction  $\Phi$  or the particle Reynolds number  $Re_p$  appear too small to be of significant influence here, the latter being in fact the consequence of differing viscosities in the bulk of the simulation. Tab. II also shows the viscosities computed for the different lubrication models at the resolutions  $R = 2$  and 8. For  $R = 2$ , the viscosities are clearly reduced with respect to  $R = 4$ , in the case of the link-based model to only 50%. Changing the resolution to  $R = 8$  increases the viscosity by about 12% for the full contact-based model while at  $R = 2$  a reduction by 21% is seen. If the Stokesian dynamics results are assumed to represent the correct viscosities, both increasing  $R$  to 8 and decreasing  $h_c$  to 0.001 slightly improves the accuracy of the present model. From the only small improvement induced by already considerable changes of  $R$  and  $h_c$  it can be concluded, however, that the viscosities obtained with the present parameters are already close to the value theoretically achieved for  $h_c = 0$  and infinite resolution. While doubling the spatial resolution in an LB simulation at fixed  $\tau$  increases the computational effort by a factor of  $2^5 = 32$ , also reducing the short-range cut-off to  $h_c = 0.001$  moderately increases the computational cost by demanding each LB time step to be subdivided in 20 instead of 10 sub-steps for the particle update in order to keep the simulation stable. Compared to other three-dimensional LB suspension models [25, 26] at even higher resolution, the present approach performs well in reproducing the viscosity already in well-affordable sim-

$h_c^{(*)}$	$\epsilon_c^{(*)}$	model	$R_{  }$	$\Phi [10^{-2}]$	$Re_p$	$\mu_r$
0.01	100	full	2	$48.3 \pm 0.5$	0.18	$7.1 \pm 0.2$
0.1	100	full	2	$48.3 \pm 0.5$	0.18	$7.0 \pm 0.2$
0.001	1000	full	2	$48.4 \pm 0.4$	0.18	$7.0 \pm 0.2$
0.01	80	full	2	$48.4 \pm 0.4$	0.18	$7.1 \pm 0.2$
0.01	1000	full	2	$48.4 \pm 0.5$	0.18	$7.1 \pm 0.3$
0.01	100	normal only	2	$48.3 \pm 0.4$	0.20	$4.9 \pm 0.1$
0.04	100	link-based	2	$48.4 \pm 0.5$	0.12	$18.8 \pm 0.9$
0.01	100	full	4	$48.7 \pm 0.6$	0.16	$8.7 \pm 0.2$
0.01	100	normal only	4	$48.7 \pm 0.6$	0.18	$6.2 \pm 0.2$
0.04	25	link-based	4	$48.7 \pm 0.5$	0.07	$38 \pm 2$

TABLE III. Data corresponding to Tab. II for oblate spheroids with half axes  $R_{||}$  and  $R_{\perp} = 3R_{||}$ .  $Re_p$  is computed based on an average radius  $(R_{||}R_{\perp}^2)^{1/3}$ .

$h_c^{(*)}$	$\epsilon_c^{(*)}$	model	$R_{  }$	$\Phi [10^{-2}]$	$Re_p$	$\mu_r$
0.01	100	full	6	$48.5 \pm 0.4$	0.08	$7.7 \pm 0.1$
0.1	100	full	6	$48.4 \pm 0.4$	0.09	$6.9 \pm 0.1$
0.001	100	full	6	$48.5 \pm 0.4$	0.08	$7.6 \pm 0.1$
0.01	50	full	6	$48.5 \pm 0.4$	0.08	$7.6 \pm 0.1$
0.01	1000	full	6	$48.5 \pm 0.3$	0.08	$7.63 \pm 0.09$
0.01	100	normal only	6	$48.4 \pm 0.4$	0.10	$4.56 \pm 0.06$
0.04	100	link-based	6	$47.9 \pm 0.4$	0.07	$12.7 \pm 0.4$
0.01	100	full	12	$49.3 \pm 0.5$	0.07	$9.7 \pm 0.1$
0.01	100	normal only	12	$49.2 \pm 0.5$	0.09	$6.18 \pm 0.09$
0.04	25	link-based	12	$49.2 \pm 0.6$	0.04	$24.9 \pm 0.6$

TABLE IV. Data corresponding to Tab. II and Tab. III for prolate spheroids with half axes  $R_{||}$  and  $R_{\perp} = R_{||}/3$ .

ulations at  $R = 4$  and  $h_c = 0.01$  thanks to the inclusion of the non-normal lubrication corrections. Without non-normal corrections the viscosity is closest to the Stokesian dynamics results for the highest resolution  $R = 8$  and the differences to data at  $R = 2$  and  $R = 4$  suggest that the numbers would converge at even larger  $R$ . The same might be true for the link-based model but here, between  $R = 4$  and  $8$  an increase of still 40% is visible while  $\mu_r$  appears to be over-predicted already.

Fig. 10(b) and (c) display the relative viscosity of suspensions of spheroids as a function of the volume fraction for the different lubrication models. In (b) the aspect ratio is  $\Lambda = 1/3$  (oblates), in (c) it is 3 (prolates). In both cases the smaller half-axis is chosen to be 2. As expected now, the link-wise model leads to an enlarged  $\mu_r$ , disabling non-normal lubrication interactions in the contact-based model to a reduced  $\mu_r$ . For  $\Phi \gtrsim 0.3$  the full contact-based model, which is believed to be most correct, predicts a clear reduction of the viscosity of prolates as compared to spheres and of oblates as compared to prolates. The result for oblates seems inconsistent with the work of Bertevas *et al.* [13] who report for oblate

spheroids of aspect ratio 0.3 at volume fractions up to  $\Phi = 0.25$  a higher viscosity than for spheres at the same volume fraction. Unfortunately, Ref. [13] provides no data for spheroidal particles at  $\Phi > 0.25$ . One has to consider that in their work the non-singular long-range hydrodynamic interactions of particles are neglected which especially at lower volume fractions might cause particles to approach closer than they would otherwise do. This would certainly increase the viscosity. If, due to the large regions of low curvature and the increased surface area this mechanism is stronger for oblates than for spheres it could explain the inconsistency. Another possible explanation is that in the model of Bertevas *et al.* [13] the particle Reynolds number is strictly  $Re_p = 0$  while in the present LB simulation it is small but finite with  $Re_p \sim 10^{-1}$ . It is hard to explain, however, how inertia could cause a reduction of the viscosity of oblates, especially since with respect to the viscosity of sphere suspensions the method by Bertevas *et al.* [13] hardly differs from the present LB model at the respective volume fractions.

In Tab. III and Tab. IV the effect of varying the short-range parameters and the resolution on the viscosity is demonstrated at  $\Phi = 0.5$  for oblate and prolate spheroids. The influence of the short-range parameters is smaller than for spheres and only increasing  $h_c$  from 0.01 to 0.1 in the case of prolates leads to a significant change in the suspension viscosity, namely a reduction by about 10%. As for spheres, doubling the resolution leads to higher viscosities. The increase is larger for spheroids, in the case of the link-wise model it amounts to roughly 100% for oblates and prolates. The viscosities obtained from the contact-based model, both with and without non-normal corrections, increase by about 25% and 35% for oblates and prolates, respectively. This result is in line with Fig. 4 and Fig. 7 above that also demonstrate that due to their potentially smaller local curvature, a higher resolution is required for spheroids than for spheres in order to achieve a comparable degree of convergence. It is interesting to examine the influence that the choice of lubrication model has over the full range of volume fractions  $\Phi$  in Fig. 10 in the case of spheroids as compared to spheres: while for spheres no significant influence is visible for  $\Phi \lesssim 0.25$ , the contact-based model without non-normal interactions leads to a reduced viscosity for prolates already at  $\Phi \approx 0.2$  and for oblates at the same volume fractions the results of all three models differ. At larger  $\Phi$  the discrepancy between the models continues to grow. The finding is consistent with the conclusion of Bertevas *et al.* [13] stating an increased importance of tangential lubrication interactions in suspensions of oblate spheroids compared to spherical particles.

## V. CONCLUSIONS

The present paper implements a contact-based method for lubrication corrections in the spirit of Nguyen and

Ladd [27] that, thanks to taking into account all leading singular terms of the resistance matrix of the involved surfaces near contact [10, 11], is applicable also to spheroidal particles. An extension to more general but smooth particle shapes is straightforward as long as the contacts between particles are such that they would touch in single points and an efficient method for finding these contacts is known. An extension to shapes such as cylinders, that might approach in line contacts, might be achievable following the arguments of Butler and Shaqfeh [38]. Since the lubrication corrections depend on the local properties of the surfaces only, non-uniform particle dispersions with different sizes and aspect ratios can be modeled in the present implementation already.

In the case of spheres, the method shows high accuracy in the resistances of two particles near contact as compared to theoretical findings [45]. The results obtained for self-diffusion and viscosity in low Reynolds number shear flow of suspensions with volume fractions between  $\Phi = 0.1$  and  $0.5$  are highly consistent with Stokesian dynamics simulations [40, 42]. For these results, a resolution of the sphere radius with  $R = 4$  lattice sites suffices. For spheroids, the respective results appear consistent when comparing simulations at different resolutions but due to the possibly smaller local radii of curvature, discretization errors play a larger role than for spheres and resolving the smaller half-axis with only 1 lattice unit cannot be recommended. For volume fractions  $\Phi \gtrsim 0.3$ , the model predicts a reduction of the suspension viscosity of prolates with aspect ratio  $\Lambda = 3$  as compared to spheres and a further reduction of oblates with aspect ratio  $1/3$  as compared to prolates.

Neglecting the non-normal lubrication corrections, as it is done by many authors simulating spherical particles [24, 25, 43], leads to an under-estimation of shear-induced diffusion and viscosity. A link-wise method for lubrication correction, similar to the initial work by Ding and Aidun [31], that over-predicts all non-normal lubrication interactions, effects an over-estimation of shear-induced diffusion and suspension viscosity. The error in the diffusion coefficient is seen for all volume fractions  $\Phi$ . This is no surprise since it is known that shear-induced diffusion can critically depend on the short-range interactions of particles [49] and already small inconsistencies summed up over many encounters can result in considerable errors in the long-time behavior of the mean-square displacement. Remarkably, the diffusion coefficients computed from the full contact-based model at a resolution as low as  $R = 2$  appear more consistent with diffusion coefficients from the same method at higher resolution and from Stokesian dynamics simulations than the ones from any of the other two methods tested at  $R = 8$ . The viscosity of spheres only slowly starts to depend on the

non-normal corrections around  $\Phi = 0.3$ . For spheroids, however, an effect is found already around  $\Phi = 0.2$ . It can be concluded that while non-normal lubrication corrections might indeed be of only minor importance for some simulations involving spheres, their proper consideration is essential, even at comparably large resolutions, such as  $R = 8$  for spheres, once shear-induced diffusion of spherical or the viscosity of spheroidal particles is of interest.

## ACKNOWLEDGMENTS

The authors thank John F. Brady and Francesco Picano for fruitful discussions. Financial support is gratefully acknowledged from the TU/e High Potential Research Program. Further, the authors acknowledge computing resources from JSC Jülich (through both GSC and PRACE grants), SSC Karlsruhe, and HLRS Stuttgart.

## Appendix: Diverging elements of $\mathbf{K}$

The diverging elements of  $\mathbf{K}$  that can be computed from the local curvatures alone are directly taken from Cox [10] and listed below only for completeness. The remaining elements that depend also on  $\Gamma_{0-3}$  and  $\Gamma'_{0-3}$  and on the coefficients of a fourth-order expansion can, in principle, be obtained by comparing the negative forces and torques on the fluid as presented by Claeys and Brady [11] with Eq. 21. However, it has been noted [50] that the derivations of the remaining diverging elements [11] suffer from a sign error that propagates into the equations (2.19a) to (2.20) of Ref. [11]. In consequence, the signs of (2.19c-d) are flipped; (2.19a-b) and (2.20) are affected in a more complex way. Following Staben *et al.* [50] it is straightforward to recalculate (2.19a-d) in the general case from which Eq. A.3, Eq. A.7, Eq. A.11, and Eq. A.12 below are obtained. The results are verified by the fact that following the same procedure while imposing the original sign error [11, 50] yields exactly the original terms [11]. Assuming particle  $j$  in Eq. 21 to be a flat wall with velocity  $\mathbf{V}_j = \mathbf{0}$  lets Eq. A.11 produce a force or torque identical to equations (2.12b) or (2.16a) in the work by Staben *et al.* [50]. Unfortunately, Eq. A.7 results in just the opposite of (2.15b) or (2.16b) of Ref. [50]. It is believed that this is caused either by a typographical error or by an inconsistency in Ref. [50] with respect to whether the equations describe the effect on the fluid by the particle or vice versa. A recalculation of (2.20) [11] would be considerably more involved [11, 50] and is therefore omitted which means that the  $\ln h$  contribution in Eq. A.10 is missing which at small  $h$ , however, is dominated by the  $h^{-1}$  term anyway.

$$K_{11} = \frac{-\pi \ln h}{\sqrt{\lambda_1 \lambda_2} S_1^2} \left[ \frac{3 \cos^2 \chi (1 - \lambda_1 S_1)^2}{(3\lambda_1 + 2\lambda_2)\lambda_1} + \frac{3 \sin^2 \chi (1 - \lambda_2 S_1)^2}{(2\lambda_1 + 3\lambda_2)\lambda_2} + S_1^2 \right] \quad (\text{A.1})$$

$$K_{12} = K_{21} = \frac{3\pi \ln h}{\sqrt{\lambda_1 \lambda_2} S_1 S_2} \sin \chi \cos \chi \left[ \frac{(1 - \lambda_1 S_1)(1 - \lambda_1 S_2)}{(3\lambda_1 + 2\lambda_2)\lambda_1} - \frac{(1 - \lambda_2 S_1)(1 - \lambda_2 S_2)}{(2\lambda_1 + 3\lambda_2)\lambda_2} \right] \quad (\text{A.2})$$

$$K_{13} = K_{31} = \frac{-3\pi \ln h}{2\sqrt{\lambda_1 \lambda_2}(\lambda_1 + \lambda_2)} \times \left[ \left[ 2\sqrt{\lambda_1}(3\kappa_0\lambda_1 + \kappa_2\lambda_2) - \frac{3}{2S_1\sqrt{\lambda_1}}((7\lambda_1 + 2\lambda_2)\kappa_0 + (\lambda_1 + 2\lambda_2)\kappa_2) \right] \frac{\cos \chi}{3\lambda_1 + 2\lambda_2} + \left[ 2\sqrt{\lambda_2}(\kappa_1\lambda_1 + 3\kappa_3\lambda_2) - \frac{3}{2S_1\sqrt{\lambda_2}}((2\lambda_1 + \lambda_2)\kappa_1 + (2\lambda_1 + 7\lambda_2)\kappa_3) \right] \frac{\sin \chi}{2\lambda_1 + 3\lambda_2} + 3\Gamma_0 \left( \frac{\cos^2 \chi}{\lambda_1} + \frac{\sin^2 \chi}{\lambda_2} \right) + 2\Gamma_1 \sin \chi \cos \chi \left( \frac{1}{\lambda_2} - \frac{1}{\lambda_1} \right) + \Gamma_2 \left( \frac{\sin^2 \chi}{\lambda_1} + \frac{\cos^2 \chi}{\lambda_2} \right) \right] \quad (\text{A.3})$$

$$K_{14} = K_{41} = \frac{3\pi \ln h}{\sqrt{\lambda_1 \lambda_2} S_1} \sin \chi \cos \chi \left[ \frac{1 - \lambda_1 S_1}{(3\lambda_1 + 2\lambda_2)\lambda_1} - \frac{1 - \lambda_2 S_1}{(2\lambda_1 + 3\lambda_2)\lambda_2} \right] \quad (\text{A.4})$$

$$K_{15} = K_{51} = \frac{3\pi \ln h}{\sqrt{\lambda_1 \lambda_2} S_1} \left[ \frac{\cos^2 \chi (1 - \lambda_1 S_1)}{(3\lambda_1 + 2\lambda_2)\lambda_1} + \frac{\sin^2 \chi (1 - \lambda_2 S_1)}{(2\lambda_1 + 3\lambda_2)\lambda_2} \right] \quad (\text{A.5})$$

$$K_{22} = \frac{-\pi \ln h}{\sqrt{\lambda_1 \lambda_2} S_2^2} \left[ \frac{3 \sin^2 \chi (1 - \lambda_1 S_2)^2}{(3\lambda_1 + 2\lambda_2)\lambda_1} + \frac{3 \cos^2 \chi (1 - \lambda_2 S_2)^2}{(2\lambda_1 + 3\lambda_2)\lambda_2} + S_2^2 \right] \quad (\text{A.6})$$

$$K_{23} = K_{32} = \frac{-3\pi \ln h}{2\sqrt{\lambda_1 \lambda_2}(\lambda_1 + \lambda_2)} \times \left[ \left[ -2\sqrt{\lambda_1}(3\kappa_0\lambda_1 + \kappa_2\lambda_2) + \frac{3}{2S_2\sqrt{\lambda_1}}((7\lambda_1 + 2\lambda_2)\kappa_0 + (\lambda_1 + 2\lambda_2)\kappa_2) \right] \frac{\sin \chi}{3\lambda_1 + 2\lambda_2} + \left[ 2\sqrt{\lambda_2}(\kappa_1\lambda_1 + 3\kappa_3\lambda_2) - \frac{3}{2S_2\sqrt{\lambda_2}}((2\lambda_1 + \lambda_2)\kappa_1 + (2\lambda_1 + 7\lambda_2)\kappa_3) \right] \frac{\cos \chi}{2\lambda_1 + 3\lambda_2} + 3\Gamma_3 \left( \frac{\sin^2 \chi}{\lambda_1} + \frac{\cos^2 \chi}{\lambda_2} \right) + 2\Gamma_2 \sin \chi \cos \chi \left( \frac{1}{\lambda_2} - \frac{1}{\lambda_1} \right) + \Gamma_1 \left( \frac{\cos^2 \chi}{\lambda_1} + \frac{\sin^2 \chi}{\lambda_2} \right) \right] \quad (\text{A.7})$$

$$K_{24} = K_{42} = \frac{-3\pi \ln h}{\sqrt{\lambda_1 \lambda_2} S_2} \left[ \frac{\sin^2 \chi (1 - \lambda_1 S_2)}{(3\lambda_1 + 2\lambda_2)\lambda_1} + \frac{\cos^2 \chi (1 - \lambda_2 S_2)}{(2\lambda_1 + 3\lambda_2)\lambda_2} \right] \quad (\text{A.8})$$

$$K_{25} = K_{52} = \frac{3\pi \ln h}{\sqrt{\lambda_1 \lambda_2} S_2} \sin \chi \cos \chi \left[ -\frac{1 - \lambda_1 S_2}{(3\lambda_1 + 2\lambda_2)\lambda_1} + \frac{1 - \lambda_2 S_2}{(2\lambda_1 + 3\lambda_2)\lambda_2} \right] \quad (\text{A.9})$$

$$K_{33} = \frac{3\pi}{h\sqrt{\lambda_1 \lambda_2}(\lambda_1 + \lambda_2)} \quad (\text{A.10})$$

$$K_{34} = K_{43} = \frac{9\pi \ln h}{4\sqrt{\lambda_1 \lambda_2}(\lambda_1 + \lambda_2)} \left[ \frac{(2\lambda_1 + \lambda_2)\kappa_1 + (2\lambda_1 + 7\lambda_2)\kappa_3}{\sqrt{\lambda_2}(2\lambda_1 + 3\lambda_2)} \cos \chi - \frac{(\lambda_1 + 2\lambda_2)\kappa_2 + (7\lambda_1 + 2\lambda_2)\kappa_0}{\sqrt{\lambda_1}(3\lambda_1 + 2\lambda_2)} \sin \chi \right] \quad (\text{A.11})$$

$$K_{35} = K_{53} = \frac{-9\pi \ln h}{4\sqrt{\lambda_1 \lambda_2}(\lambda_1 + \lambda_2)} \left[ \frac{(\lambda_1 + 2\lambda_2)\kappa_2 + (7\lambda_1 + 2\lambda_2)\kappa_0}{\sqrt{\lambda_1}(3\lambda_1 + 2\lambda_2)} \cos \chi + \frac{(2\lambda_1 + \lambda_2)\kappa_1 + (2\lambda_1 + 7\lambda_2)\kappa_3}{\sqrt{\lambda_2}(2\lambda_1 + 3\lambda_2)} \sin \chi \right] \quad (\text{A.12})$$

$$K_{36} = K_{63} = \frac{-3\pi \ln h}{2\sqrt{\lambda_1 \lambda_2}(\lambda_1 + \lambda_2)} \sin \chi \cos \chi \left[ \frac{1}{S_1} - \frac{1}{S_2} \right] \left[ \frac{1}{\lambda_1} - \frac{1}{\lambda_2} \right] \quad (\text{A.13})$$

$$K_{44} = \frac{-3\pi \ln h}{\sqrt{\lambda_1 \lambda_2}} \left[ \frac{\sin^2 \chi}{(3\lambda_1 + 2\lambda_2)\lambda_1} + \frac{\cos^2 \chi}{(2\lambda_1 + 3\lambda_2)\lambda_2} \right] \quad (\text{A.14})$$

$$K_{45} = K_{54} = \frac{3\pi \ln h}{\sqrt{\lambda_1 \lambda_2}} \sin \chi \cos \chi \left[ \frac{-1}{(3\lambda_1 + 2\lambda_2)\lambda_1} + \frac{1}{(2\lambda_1 + 3\lambda_2)\lambda_2} \right] \quad (\text{A.15})$$

$$K_{55} = \frac{-3\pi \ln h}{\sqrt{\lambda_1 \lambda_2}} \left[ \frac{\cos^2 \chi}{(3\lambda_1 + 2\lambda_2)\lambda_1} + \frac{\sin^2 \chi}{(2\lambda_1 + 3\lambda_2)\lambda_2} \right] \quad (\text{A.16})$$

Some of the symbols in Eq. A.1 to Eq. A.16 still require clarification. This information is accessible also in Ref. [11] and, partly, [10] but is summarized here to make the above description self-contained. As visible in Fig. 3,  $\phi$  is the angle between the axes of principal curvature  $x_1$  and  $x'_1$  and between  $x_2$  and  $x'_2$  of both surfaces. In the derivation of the singular terms, the height of the quadratically approximated gap between the surfaces defined by Eq. 19 and Eq. 20 is brought to the simple form

$$h_z = 1 + \lambda_1 \hat{x}_1^2 + \lambda_2 \hat{x}_2^2 \quad (\text{A.17})$$

in terms of rescaled coordinates  $\hat{x}_1$  and  $\hat{x}_2$  where the new principal curvatures  $\lambda_1$  and  $\lambda_2$  are the eigenvalues of the matrix

$$\begin{pmatrix} \frac{1}{2S_1} + \frac{\cos^2 \phi}{2S'_1} + \frac{\sin^2 \phi}{2S'_2} & \frac{\sin \phi \cos \phi}{2} \left( \frac{1}{S'_1} - \frac{1}{S'_2} \right) \\ \frac{\sin \phi \cos \phi}{2} \left( \frac{1}{S'_1} - \frac{1}{S'_2} \right) & \frac{1}{2S_2} + \frac{\sin^2 \phi}{2S'_1} + \frac{\cos^2 \phi}{2S'_2} \end{pmatrix}.$$

The trigonometric functions of the angle  $\chi$  that transforms between the directions of principal curvature  $x_1$  and  $x_2$  and the main axes  $\hat{x}_1$  and  $\hat{x}_2$  can be obtained from the components of the corresponding normalized eigenvectors  $\hat{\mathbf{I}}_1$  and  $\hat{\mathbf{I}}_2$ , which form the transformation matrix, for instance

$$\hat{\mathbf{I}}_2 = \begin{pmatrix} \sin \chi \\ \cos \chi \end{pmatrix}. \quad (\text{A.18})$$

The  $\kappa_{0-3}$  describe the cubic features of both surfaces in the coordinate frame defined by  $\hat{x}_1$  and  $\hat{x}_2$ . Knowing  $\phi$ ,

it is possible to express the cubic terms, characterized by  $\Gamma'_{0-3}$  in Eq. 20, in the principal frame  $x_1$  and  $x_2$  of the other surface. The transformation can be described by a set of 4 functions  $m_i(\alpha, a_0, a_1, a_2, a_3)$  of a transformation angle  $\alpha$  and a set of cubic coefficients  $a_{0-3}$  defined as

$$\begin{aligned} m_0 &= a_0 \cos^3 \alpha - a_1 \sin \alpha \cos^2 \alpha \\ &\quad + a_2 \sin^2 \alpha \cos \alpha - a_3 \sin^3 \alpha \\ m_1 &= a_0 3 \sin \alpha \cos^2 \alpha + a_1 (\cos^3 \alpha - 2 \sin^2 \alpha \cos \alpha) \\ &\quad + a_2 (\sin^3 \alpha - 2 \sin \alpha \cos^2 \alpha) + a_3 3 \sin^2 \alpha \cos \alpha \\ m_2 &= a_0 3 \cos \alpha \sin^2 \alpha + a_1 (2 \cos^2 \alpha \sin \alpha - \sin^3 \alpha) \\ &\quad + a_2 (\cos^3 \alpha - 2 \cos \alpha \sin^2 \alpha) - a_3 (3 \cos^2 \alpha \sin \alpha) \\ m_3 &= a_0 \sin^3 \alpha + a_1 \cos \alpha \sin^2 \alpha \\ &\quad + a_2 \cos^2 \alpha \sin \alpha + a_3 \cos^3 \alpha \end{aligned} \quad (\text{A.19})$$

and then reads

$$\beta_i = m_i(\phi, \Gamma'_0, \Gamma'_1, \Gamma'_2, \Gamma'_3). \quad (\text{A.20})$$

The same functional dependency is used to transform the added cubic coefficients  $k_i = \Gamma_i + \beta_i$  into the frame of  $\hat{x}_1$  and  $\hat{x}_2$ . The rescaled coordinates demand rescaling also of the cubic coefficients to obtain

$$\kappa_i = \frac{m_i(\chi, k_0, k_1, k_2, k_3)}{\sqrt{\lambda_1}^{3-i} \sqrt{\lambda_2}^i}. \quad (\text{A.21})$$

[1] M. Lopez and M. D. Graham, *Physics of Fluids* **19**, 073602 (2007).

[2] J. R. Clausen, D. A. Reasor, and C. K. Aidun, *Journal of Fluid Mechanics* **685**, 202 (2011).

[3] T. Krüger, *Computer simulation study of collective phenomena in dense suspensions of red blood cells under shear*, Ph.D. thesis, Ruhr-Universität Bochum (2012).

[4] H. Zhao, E. S. G. Shaqfeh, and V. Narsimhan, *Physics of Fluids* **24**, 011902 (2012).

- [5] X. Grandchamp, G. Couplier, A. Srivastav, C. Minetti, and T. Podgorski, *Phys. Rev. Lett.* **110**, 108101 (2013).
- [6] T. Omori, T. Ishikawa, Y. Imai, and T. Yamaguchi, *J. Fluid Mech.* **724**, 154 (2013).
- [7] K. Yeo and M. R. Maxey, *Physics of Fluids* **25**, 053303 (2013).
- [8] B. Metzger, P. Pham, and J. E. Butler, *Phys. Rev. E* **87**, 052304 (2013).
- [9] A. Goldman, R. Cox, and H. Brenner, *Chemical Engineering Science* **22**, 637 (1967).
- [10] R. G. Cox, *International Journal of Multiphase Flow* **1**, 343 (1974).
- [11] I. L. Claeyss and J. F. Brady, *PhysicoChem. Hydrodyn* **11**, 261 (1989).
- [12] I. L. Claeyss and J. F. Brady, *J. Fluid Mech.* **251**, 411 (1993).
- [13] E. Bertevas, X. Fan, and R. I. Tanner, *Rheol. Acta* **49**, 53 (2010).
- [14] S. Succi, *The Lattice Boltzmann Equation for Fluid Dynamics and Beyond*, Numerical Mathematics and Scientific Computation (Oxford University Press, 2001).
- [15] A. J. C. Ladd, *J. Fluid Mech.* **271**, 285 (1994).
- [16] A. J. C. Ladd, *J. Fluid Mech.* **271**, 311 (1994).
- [17] A. J. C. Ladd and R. Verberg, *J. Stat. Phys.* **104**, 1191 (2001).
- [18] C. K. Aidun and J. R. Clausen, *Annu. Rev. Fluid Mech.* **42**, 439 (2010).
- [19] C. Kunert, J. Harting, and O. I. Vinogradova, *Phys. Rev. Lett.* **105**, 016001 (2010).
- [20] C. Kunert and J. Harting, *IMA Journal of Applied Mathematics* **76**, 761 (2011).
- [21] S. Schwarzer, *Phys. Rev. E* **52**, 6461 (1995).
- [22] M. Hecht, J. Harting, T. Ihle, and H. J. Herrmann, *Phys. Rev. E* **72**, 011408 (2005).
- [23] N. S. Martys, *Journal of Rheology* **49**, 401 (2005).
- [24] A. J. C. Ladd, *Physics of Fluids* **9**, 491 (1997).
- [25] J. Hyväluoma, P. Raiskinmäki, A. Koponen, M. Kataja, and J. Timonen, *J. Stat. Phys.* **121**, 149 (2005).
- [26] J. Kromkamp, D. T. M. van den Ende, D. Kandhai, R. G. M. van der Sman, and R. M. Boom, *Chemical engineering science* **61**, 858 (2006).
- [27] N.-Q. Nguyen and A. J. C. Ladd, *Phys. Rev. E* **66**, 046708 (2002).
- [28] D. Qi, L. Luo, R. Aravamuthan, and W. Strieder, *J. Stat. Phys.* **107**, 101 (2002).
- [29] F. Günther, F. Janoschek, S. Frijters, and J. Harting, *Computers & Fluids* **80**, 184 (2013).
- [30] F. Janoschek, F. Toschi, and J. Harting, *Phys. Rev. E* **82**, 056710 (2010).
- [31] E.-J. Ding and C. K. Aidun, *J. Stat. Phys.* **112**, 685 (2003).
- [32] R. M. MacMeccan, J. R. Clausen, G. P. Neitzel, and C. K. Aidun, *Journal of Fluid Mechanics* **618**, 13 (2009).
- [33] J. R. Clausen, *The effect of particle deformation on the rheology and microstructure of noncolloidal suspensions*, Ph.D. thesis, Georgia Institute of Technology (2010).
- [34] Y. H. Qian, D. d'Humières, and P. Lallemand, *Europhys. Lett.* **17**, 479 (1992).
- [35] C. K. Aidun, Y. Lu, and E.-J. Ding, *J. Fluid Mech.* **373**, 287 (1998).
- [36] F. Janoschek, F. Toschi, and J. Harting, *Macromolecular Theory and Simulations* **20**, 562 (2011).
- [37] A. Lin and S.-P. Han, *SIAM Journal on Optimization* **13**, 298 (2002).
- [38] J. E. Butler and E. S. G. Shaqfeh, *J. Fluid Mech.* **468**, 205 (2002).
- [39] A. Komnik, J. Harting, and H. J. Herrmann, *Journal of Statistical Mechanics: theory and experiment* **P12003** (2004).
- [40] A. Sierou and J. F. Brady, *Journal of Fluid Mechanics* **506**, 285 (2004).
- [41] R. C. Ball and J. R. Melrose, *Advances in colloid and interface science* **59**, 19 (1995).
- [42] A. Sierou and J. F. Brady, *Journal of Rheology* **46**, 1031 (2002).
- [43] S. Frijters, F. Günther, and J. Harting, *Soft Matter* **8**, 6542 (2012).
- [44] A. R. Thornton, T. Weinhart, V. Ogarko, and S. Luding, *Computer methods in materials science* **13**, 197 (2013).
- [45] D. J. Jeffrey and Y. Onishi, *J. Fluid Mech.* **139**, 261 (1984).
- [46] S. Kim and S. J. Karrila, *Microhydrodynamics: principles and selected applications* (Dover Publications Inc., New York, 2005).
- [47] J. R. Clausen, D. A. Reasor Jr., and C. K. Aidun, *Computer Physics Communications* **181**, 1013 (2010).
- [48] E. Lorenz, A. G. Hoekstra, and A. Caiazzo, *Phys. Rev. E* **79**, 036706 (2009).
- [49] F. R. da Cunha and E. J. Hinch, *J. Fluid Mech.* **309**, 211 (1996).
- [50] M. E. Staben, A. Z. Zinchenko, and R. H. Davis, *J. Fluid Mech.* **553**, 187 (2006).